Correspondence to:
G. Le Gland,
guillaume.legland@free.fr

An Estimate of Thorium 234 Partition Coefficients Through Global Inverse Modeling

Guillaume Le Gland[1] (iD), **Olivier Aumont[2]** (iD)**, and Laurent Mémery[1]** (iD)

[1]LEMAR, Institut Universitaire Européen de la Mer, Plouzané, France, [2]LOCEAN, Institut Pierre Simon Laplace, Paris, France

Abstract Thorium-234 (^{234}Th), an insoluble radioisotope scavenged by marine particles, can be used as a proxy of the biological carbon pump. Thorium-234 observations can constrain biogeochemical models, but a necessary first step is to estimate the poorly known partition coefficients between particulate and dissolved phases. In this study, the ^{234}Th partition coefficients for five particle types, differing in size and chemical composition, are estimated by fitting a global 3-D ^{234}Th model based on the coupled ocean general circulation-biogeochemistry model NEMO-PISCES (at a resolution of 2°) to a global ^{234}Th data set (including GEOTRACES data). Surface partition coefficients are estimated between 0.79 and 16.7×10^6. Biogenic silica has the smallest partition coefficients. Small particulate organic carbon and lithogenic dust have the largest. Thorium-234 observations at depth cannot be recovered without allowing partition coefficients to increase by one order of magnitude from surface to 1,000 m deep. In our time-dependent global 3-D model, the biases introduced by three common assumptions made in biological carbon pump studies can be quantified. First, using the C:^{234}Th ratio of large particles alone leads to an overestimation of carbon export at the base of the euphotic layer, by up to a factor 2. Furthermore, assuming steady state and neglecting transport by advection and diffusion can bias fluxes by as much as 50%, especially at high latitudes and in upwellings, with a sign and intensity depending on the season.

1. Introduction

The biogeochemical cycles of carbon and macronutrients (nitrogen, phosphorus, and silicon) are complex, depending on many sources and sinks, associated with biological (photosynthesis, respiration, …), chemical (dissolution, adsorption, …), and physical (sedimentation, aggregation, …) processes. The distribution of these elements cannot be directly related to specific sources or sinks. In contrast, some trace elements and isotopes (TEIs) are affected by a relatively small number of sources and sinks. This is why their distribution contains workable information on key oceanic processes.

The international program GEOTRACES has been designed to improve our knowledge on TEIs cycles and the oceanic processes controlling their distribution, by means of observations, modeling, and laboratory experiments. Since 2006, tens of TEIs have been measured by GEOTRACES oceanographic cruises. Some of them are studied because they constitute essential micronutrients for life in the ocean, such as iron (Fe), zinc (Zn), and copper (Cu). Others, on the contrary, are pollutants, such as lead (Pb) and cadmium (Cd). Finally, several TEIs are used as proxies because of their relatively simple behavior in the ocean. For instance, radium-228 is a proxy of submarine groundwater discharge (Kwon et al., 2014; Le Gland et al., 2017; Moore et al., 2008), and the neodymium isotope ratio is related to the exchange between continental margins and open ocean (Jeandel et al., 2007). One trace isotope of particular interest is thorium-234 (^{234}Th), a proxy of particle fluxes to the deep ocean. Thorium-234 has often been used to estimate a key flux in the global carbon cycle, the biological carbon pump (BCP).

The BCP is defined as the biological flux of detritic carbon from the ocean surface to the ocean interior (Volk & Hoffert, 1985). It is composed of a soft-tissue pump, exporting organic carbon produced by phytoplankton through photosynthesis, and a carbonate pump, where the exported particles are inorganic carbon compounds, chiefly calcium carbonate ($CaCO_3$), produced by some marine organisms including coccolithophores and foraminifera. Depending on the depth reached by the sinking particles before remineralization, carbon is sequestered from a few years (close to surface) to submillenium time scales, which is the time required for meridional overturning circulation to bring deep waters back to the surface (DeVries

& Primeau, 2011; DeVries et al., 2012). The BCP is an important part of the natural carbon cycle. It might decrease in the future due to global warming (Wohlers et al., 2009). The precise intensity of the BCP is still poorly known. Laws et al. (2000) used field estimates, most of them based on nitrate uptake, to relate carbon export to total primary production and sea surface temperature (SST). The BCP was then extrapolated using satellite data of sea surface temperature and primary production, producing a global estimate of 11 GtC/year. But the BCP can also be estimated using ^{234}Th deficit. Henson et al. (2011) found a much lower value of 5 GtC/year using this approach.

Thorium-234 is related to the BCP because of its low solubility. It is produced by the radioactive decay of uranium-238 (^{238}U). As ^{238}U is soluble in seawater and has a half-life of 4.47×10^9 year, far longer than any oceanic process, it is distributed in the ocean in a nearly uniform way. Uranium-238 concentration was shown to be proportional to salinity (Chen et al., 1986), because evaporation and precipitation concentrate and dilute the two solutes in the same way. If it were conservative, ^{234}Th would be at secular equilibrium with ^{238}U, that is, both isotopes would have the same activity, around 2,500 dpm/m^3. However, being insoluble, thorium is adsorbed onto sinking particles and removed from the upper layer, creating a deficit compared to ^{238}U, at least in the upper 100 m of the ocean. Observations of this deficit can be used to estimate ^{234}Th export. The ^{234}Th export flux being known, the carbon export is estimated by taking into account the carbon to thorium (C:^{234}Th) ratio of sinking particles.

Hundreds of local carbon export estimates have been produced using one-box models of ^{234}Th deficit (Le Moigne et al., 2013). As ^{234}Th decays with a half-life of 24.1 days, information integrated over several weeks is available using only one profile. The full export flux $F(z)$ at a depth z is

$$F(z) = \int_0^z \left[\lambda_{Th}(U - Th) - \frac{\partial Th}{\partial t} - T \right] dz. \tag{1}$$

In this equation, $\lambda_{Th} = \frac{ln2}{t_{1/2}} = 2.88 \times 10^{-2}$ day^{-1} is the decay constant of ^{234}Th, $\frac{\partial Th}{\partial t}$ represents tendency, and T stands for transport by advection and diffusion. $F(z)$ is usually estimated between 100 and 150 m. Transport is the most difficult term to estimate, as it depends on ^{234}Th activity gradients, seawater speed, and diffusivity. It is often neglected. Tendency is another commonly neglected term. Tendency can be estimated by sampling twice at the same location in a few weeks (Buesseler et al., 1998). But in most cases, this approach is not applied because repeated occupation of the same station is considered too expensive and incompatible with the logistics of most open ocean cruises (Savoye et al., 2006). Instead, a simplified ^{234}Th export flux, $F_{SS}(z)$, based solely on the ^{234}Th cumulated deficit from the surface to the depth z, is computed:

$$F_{SS}(z) = \int_0^z \lambda_{Th}(U - Th)dz. \tag{2}$$

The ^{234}Th export flux can be converted into a particle export flux if the amount of ^{234}Th adsorbed on particles is known. The affinity of ^{234}Th for particles is represented by a dimensionless number, the partition coefficient, or K^d, defined as the ratio of ^{234}Th activity on particles to ^{234}Th activity in seawater, normalized by the particle concentration:

$$K^d = \frac{Th_p}{Th_d C_p}. \tag{3}$$

In the above equation, Th_p is the activity of particulate ^{234}Th per volume of seawater (in dpm/m^3), Th_d is the activity of dissolved ^{234}Th per volume of seawater (in dpm/m^3), and C_p is the mass concentration of particles (in kg/kg). The partition coefficient is often measured and used in models because, at equilibrium and under the assumption that adsorption, desorption, and particle dissolution have first-order kinetics, K^d is a constant, depending only on the nature of particles. The partition coefficient of each particle type then provides an information on the global behavior of oceanic ^{234}Th. Studies have documented a large variability of K^d in the ocean. The chemical composition of particles is generally considered to be the most important explanatory factor. Partition coefficients of different particle types have been determined both in the laboratory (Chuang et al., 2013; Lin et al., 2015) and using in situ data (Hayes et al., 2015; Roy-Barman et al., 2005). The particle types generally considered in these studies are organic molecules, opal, calcite, and several metal oxides including manganese oxide. K^d estimates are generally in the broad range from 10^4 to

10^9 and differ from study to study, even for the same particle types. Particle size is also considered to have an impact on partition coefficients, but this has been far less investigated. In situ measurements sometimes include two operationally defined size classes of particles. In this case, the division between small and large particles corresponds to filter size, for example, 53 or 70 μm (Buesseler et al., 1995; Cochran et al., 2000). Smaller particles are expected to have a larger K^d because of their higher surface to volume ratio, and this has sometimes been evidenced (Charette & Moran, 1999; Planchon et al., 2013). But in some other cases, the contrary has been observed (Buesseler et al., 1995; Moran et al., 2003). There is thus no consensus on the effect of particle size on K^d.

The partition coefficients of the particle types containing carbon are closely related to the C:^{234}Th ratio, which is used in local studies to compute the carbon export flux. Simplifications are often used to estimate C:^{234}Th. In many cases, only particles larger than 53 μm, collected by in situ pumps, are considered. This approach is accurate only if smaller particles have a similar K^d or if these are negligible contributors to the ^{234}Th export flux. In order to use ^{234}Th as a proxy of the BCP, the phases carrying and exporting this isotope must be identified first.

The present study is designed to improve the estimates of the BCP through a better knowledge of thorium reactivity. An entirely new approach, three-dimensional time-dependent inverse modeling, is used to provide global estimates of ^{234}Th partition coefficients for several particle types. Indeed, numerical modeling offers a unique opportunity to estimate the effect of transport and unsteadiness on the distribution of ^{234}Th and to separate the contributions of different particle types to scavenging. These features enable us to evaluate the biases that simplifications of the thorium cycle can induce on carbon export estimates and to diagnose model errors in particle dynamics. This article is organized as follows. In section 2, we describe the three main requirements of our inverse model: a global data set, a forward model of ^{234}Th behavior, and an inverse algorithm. A detailed list of simulations is also provided. Section 3 presents the main results: the sensitivity of ^{234}Th concentrations to each K^d, the optimized K^d values and their uncertainties, and the residuals after inversion. Results are presented for several inversions. Section 4 compares our partition coefficients with previous studies, clarifies the implications of our results for the use of ^{234}Th as a proxy of the BCP, and discusses the limitations and possible improvements of our approach.

2. Methods

2.1. Thorium 234 Data Set

The first requirement of the inversion technique is a global data set of ^{234}Th concentrations. In fact, for reasons of comparability with other isotopes, the measured quantity is the amount of radioactivity per unit of volume, called activity and expressed in disintegrations per minute per cubic meter or dpm/m^3. For a given isotope, the activity is the product of the concentration and the radioactive decay constant. Since 1969 (Matsumoto, 1975), ^{234}Th activity has been measured by tens of oceanographic cruises. The data set used in this study (detailed in supporting information Data Set S1) includes data from the literature (Amiel et al., 2002; Buesseler et al., 1995, 2009; Charette & Moran, 1999, Charette et al., 1999; Coale & Bruland, 1985; Coppola et al., 2002; Jacquet et al., 2011; Kawakami & Honda, 2007; Knauss et al., 1978; Moran et al., 2003; Morris et al., 2007; Murray et al., 1989; Roca-Martí et al., 2017; Rodriguez y Baena et al., 2008; Santschi et al., 1999; Shimmield et al., 1995; Thomalla et al., 2006; Zhou et al., 2012), PANGAEA data publisher (Buesseler, 2003a, 2003b, 2003c; Cochran & Cochran, 2003; Coppola & Jeandel, 2004; JGOFS-INDIA, 2002, 2013; Moran et al., 2012; Roca-Martí et al., 2016; Rutgers van der Loeff, 2007; Young & Murray, 2003), and five GEOTRACES cruises whose data are reported in the Intermediate Data Product 2014 (Mawji, 2015): GA02 (Owens et al., 2014) in the western Atlantic, GA03 (Owens et al., 2014) from the United States to Cape Verde to Portugal, GIPY11 (Cai et al., 2010) in the Arctic Ocean, and GIPY4 (Planchon et al., 2013) and GIPY5 (Rutgers van der Loeff et al., 2011) in the Atlantic sector of the Southern Ocean. In a near future, GEOTRACES data from all major oceanic basins should be available. As observations deeper than 1,000 m are scarce and potentially affected by hydrothermal vents (German et al., 1991) or nepheloid layers (Bacon & Rutgers van der Loeff, 1989) , our data set has been restricted to data shallower than 1,000 m.

The data set is composed of 5,361 observations of total ^{234}Th activity (Figure 1) from the surface to 1,000 m deep, 1,581 of which are divided into a dissolved and one or two particulate pools. A number of 1,619 are shallower than 50 m, 1,193 are between 50 and 100 m deep, 1,722 are between 100 and 300 m deep, and 827 are between 300 and 1,000 m deep (Figure 2). The Atlantic, Arctic, and Southern oceans have been sampled
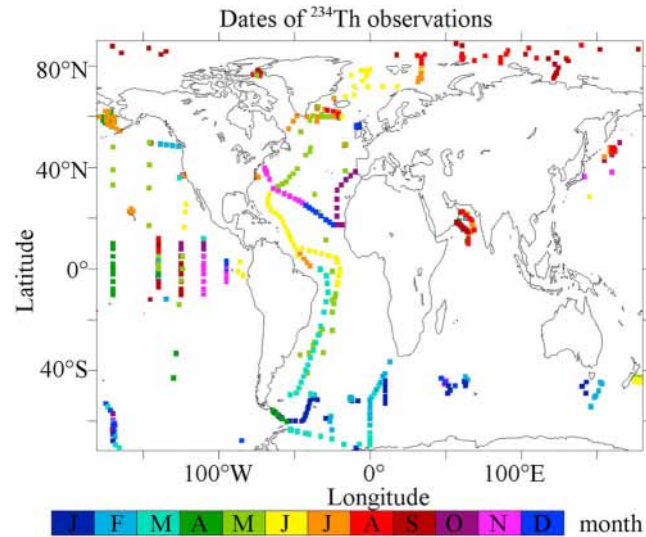
Figure 1. Location and month of the year of ^{234}Th activity observations.

more than the Pacific Ocean, and there are very few observations in the Indian Ocean. Globally, activities range from 280 to 3,760 dpm/m^3, with more than 90% of them between 1,200 and 2,700 dpm/m^3. Most activities deeper than 100 m are close to 2,500 dpm/m^3, which corresponds to the secular equilibrium with ^{238}U, whereas the upper 100 m tends to have lower activities of ^{234}Th, particularly at high latitudes. Measurements in the high latitudes are generally performed during Spring and Summer of the corresponding hemisphere, when biological activity is the highest.
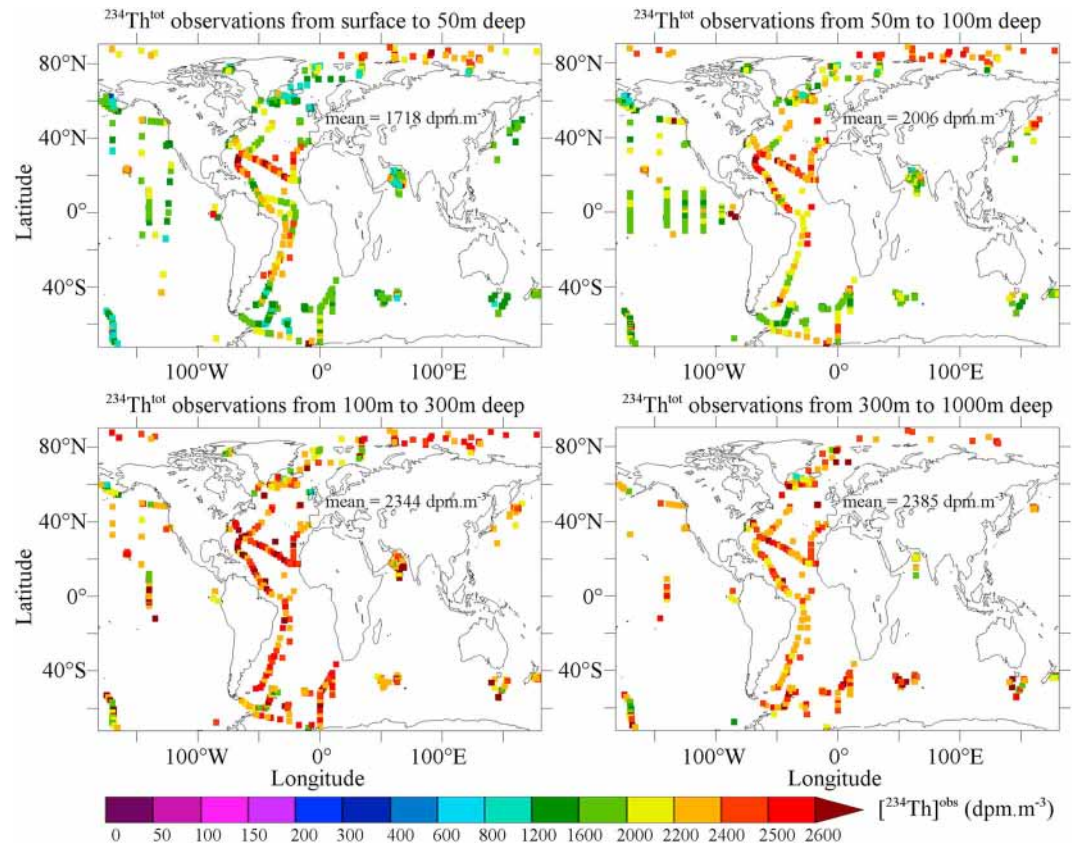

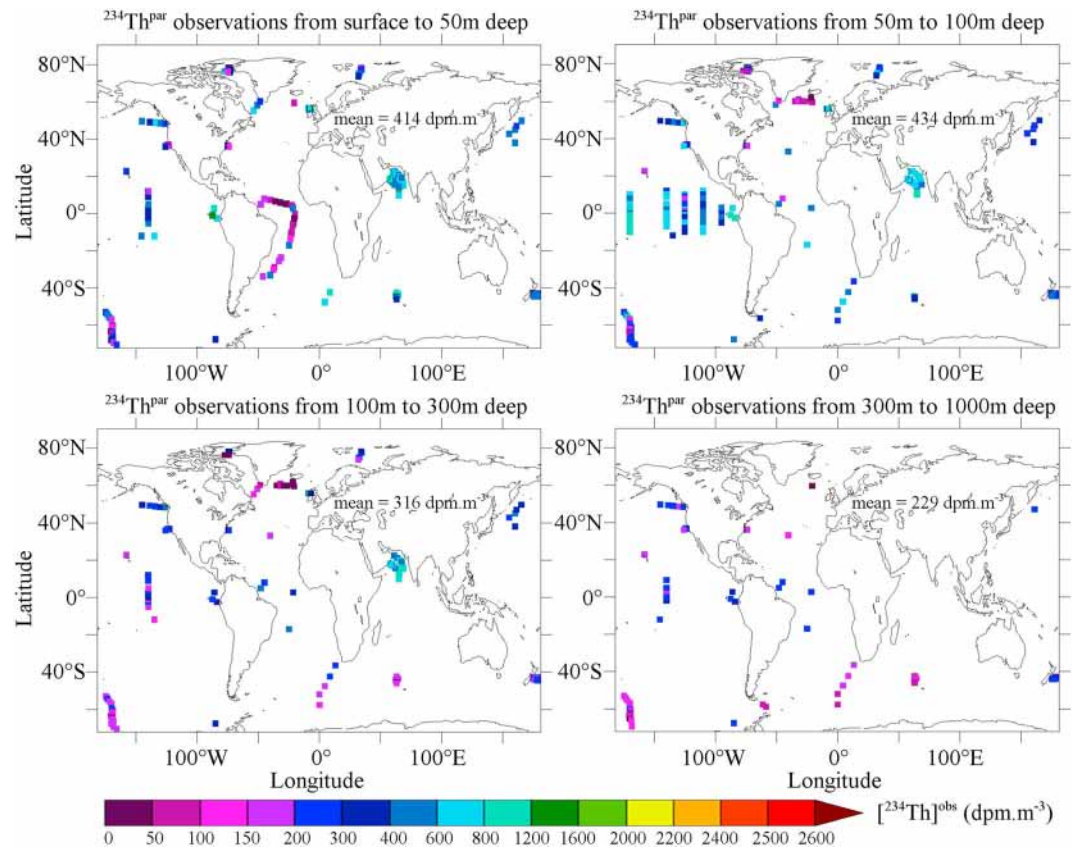**Figure 2.** Total ^{234}Th activity observations.

Figure 3. Particulate ^{234}Th activity observations.

Some cruises have also measured the ^{234}Th activity on particles. These activities lie between 10 and 2,280 dpm/m^3, with 80% of them between 100 and 800 dpm/m^3 (Figure 3). This information complements total ^{234}Th because this element is mainly adsorbed onto small particles, whereas particle export and thus the total thorium deficit are thought to be caused mainly by large particles that sink faster (Bishop et al., 1977; Fowler & Knauer, 1986; McCave, 1975). However, it should be noted that the size limit between the dissolved and particulate phases varies between 0.2 and 1 μm (see Data Set S1), making comparisons between different observations more difficult.

2.2. Forward ^{234}Th Model

The second requirement of the inversion technique is to establish a link between the physical parameters to be estimated and the tracer activities: This is achieved through the forward model. This numerical model reproduces the spatial distribution of ^{234}Th activity based on the oceanic circulation and the sources and sinks of this isotope.

In this study, three processes impacting ^{234}Th are considered: net radioactive production (R), scavenging (S), and transport (T).

$$\frac{\partial Th_{\text{tot}}}{\partial t} = R - S + T. \tag{4}$$

Radioactivity is the best constrained process affecting ^{234}Th. Thorium-234 is produced directly in the ocean, in dissolved form, by the decay of uranium-238 (^{238}U). As ^{238}U is chemically conservative and as its half-life (4.47×10^9 years) is very long compared to the time scale of oceanic circulation (a few millenia according to DeVries & Primeau, 2011), the activity of ^{238}U should be nearly constant in the ocean. According to Chen et al. (1986), it is approximately proportional to salinity, with a ratio of 70.65 dpm·m^{-3}·psu^{-1}. Thorium-234 is then removed by its own radioactive decay with a much shorter half-life: 24.1 days. The sum of the radioactive source and sink acts as a restoring term toward the ^{238}U activity. In the absence of any other sink, radioactivity would lead to secular equilibrium: The activities of ^{238}U and ^{234}Th would be identical, around

2,500 dpm/m^3, which means that there are the same number of radioactive disintegrations creating and destroying ^{234}Th. The net radioactive production of ^{234}Th is

$$R = \lambda_{Th}(U - Th_{\text{tot}}). \tag{5}$$

Scavenging is the process that disrupts the secular equilibrium. As Th is insoluble in seawater, it is readily adsorbed onto solid particles and removed from the particle-rich euphotic layer by particle sinking. Scavenging is a much less well-understood process than radioactivity. Scavenging by particle type p depends on its sinking speed w$_p$ and its particulate ^{234}Th activity Th$_p$. The export rate of ^{234}Th is

$$S = \sum_p \frac{\partial(Th_p w_p)}{\partial z}. \tag{6}$$

Thorium-234 activity on type p depends in turn on the dissolved ^{234}Th concentration Th$_d$, the particle concentration C$_p$, and the partition coefficient of p: K_p^d. It is described by the following expression, where n is a mute index also representing particle type:

$$Th_p = K_p^d C_p Th_d = \frac{K_p^d C_p Th_{\text{tot}}}{1 + \sum_n K_n^d C_n}. \tag{7}$$

Scavenging is the only process depending on the unknowns of our inverse problem, the partition coefficients. Note that K_p^d always appears in the equations in the form of the product $K_p^d C_p$. Hence, a change in one or the other quantity has the same effect on the distribution of total ^{234}Th (through scavenging) and particulate ^{234}Th. Thus, the partition coefficient and the concentration of a given particle type cannot be estimated independently of each other.

A third term, transport by circulation, alters thorium distribution, making the link between ^{234}Th distribution and particle export less direct. For instance, horizontal transport can create a deficit in a region with little scavenging by bringing water from a neighboring region experiencing a stronger scavenging intensity. Vertical transport can reduce or deepen the surface deficit depending on its direction, potentially biasing carbon export estimates. Transport is composed of advection and diffusion, depending on water velocity $\vec{V}$ and diffusivity K, respectively:

$$T = -\vec{V}.\vec{\nabla}Th_{\text{tot}} + \vec{\nabla}.(K\vec{\nabla}Th_{\text{tot}}). \tag{8}$$

Modeling processes R, S, and T requires a 3-D model of oceanic circulation and particle dynamics. The ocean model used in this study is the NEMO 3.6 platform, using OPA 8.1 (Madec, 2015) for the general circulation and LIM3 (Vancoppenolle et al., 2009) for sea ice. An ORCA2 grid is used, with a horizontal resolution of 2° in longitude by 2° cos ϕ (where ϕ is the latitude), enhanced to 0.5° near the equator, in latitude. The mesh is tripolar in order to overcome singularities. The North Pole is replaced by two "inland poles" in the Northern Hemisphere. The ocean model has 31 vertical levels, ranging from the surface to 6,000 m deep, and the upper layers have a thickness of around 10 m. The simulation is forced by a seasonal climatological data set, based on the reanalysis from the National Centers for Environment Predictions (NCEP) and the National Centers for Environment Predictions (NCAR) reanalysis and satellite data. The particle fields used to compute scavenging are produced by a biogechemical model coupled with NEMO: Pelagic Interactions Scheme for Carbon and Ecosystem Studies (PISCES-v2) (Aumont et al., 2015) as modified by Aumont et al. (2017).

PISCES simulates the lower trophic levels of the ocean (phytoplankton and zooplankton) and the cycles of carbon, oxygen, and the main nutrients limiting phytoplankton growth (NH_4^+, NO_3^-, PO_4^{3-}, $Si(OH)_4$, and Fe). For all plankton groups, constant Redfield C/N/P ratios are imposed, but iron and silica are explicitly computed. PISCES also computes dissolved inorganic carbon, dissolved organic carbon, and sinking particles. Nutrients, chlorophyll, and alkalinity have been validated against measurements (Aumont et al., 2015). In this study, circulation and particle fields are averaged over periods of 5 days.

PISCES simulates nine particle types which are able to scavenge thorium. Four types correspond to living plankton, divided into nanophytoplankton (phy), diatoms (phy2), microzooplankton (zoo), and mesozooplankton (zoo2). Four others are detritus produced by plankton through mortality, egestion of fecal pellets,
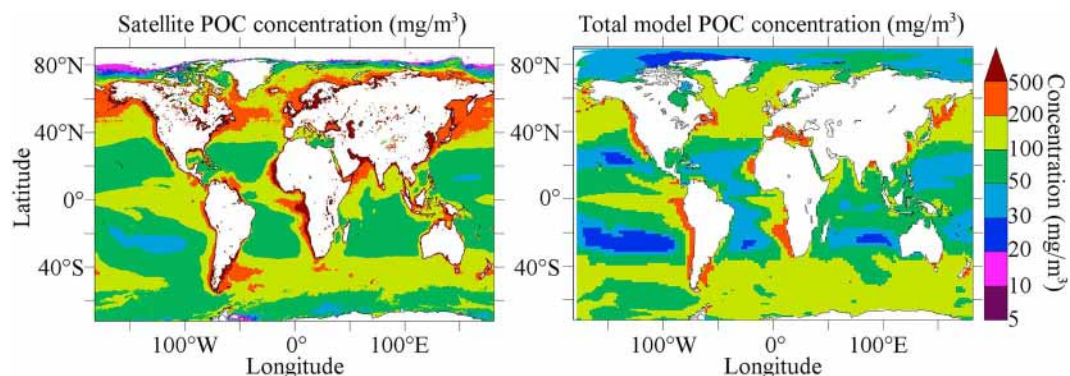
Figure 4. Yearly averaged climatology of surface POC concentration from satellite observations (http://globcolour.info) and comparison with Pelagic Interactions Scheme for Carbon and Ecosystem Studies surface organic carbon (including both the living and detritic pools). POC = particulate organic carbon.

aggregation of phytoplankton, and coagulation of dissolved organic carbon: These are particulate organic carbon (POC), divided in smaller (sPOC) and larger (bPOC) than 100-μm size classes, calcite (cal), and biogenic silica (bSi). Particulate organic carbon is modeled using the variable lability version, validated against profiles of observations from the Atlantic and Pacific basins (Aumont et al., 2017). Taking a continuum of POC lability into account increased POC concentration in the interior of the ocean by one or two orders of magnitude, making them much closer to observations than in previous model versions. PISCES surface particulate organic carbon concentration, including living organisms, is distributed in a similar way to surface POC from satellite product globcolour (Figure 4), which is also validated by in situ measurements. Cal is fueled by calcifying nanophytoplankton mortality and grazing on calcifying nanophytoplankton by both groups of zooplankton. Calcifying plankton, such as coccolithophores, is not explicitly modeled. Instead, cal production is empirically parameterized as a variable fraction of organic carbon production by nanophytoplankton. This fraction is maximal if irradiance is between 4 and 30 W/m^2, temperature is around 10 °C, the mixed layer depth is less than 50 m deep, and the water is not oligotrophic (Aumont et al., 2015). Dissolution of cal particles depends on carbonate ion concentration and only occurs in undersaturated waters, following the parameterization of Gehlen et al. (2007). bSi is fueled by diatom mortality and grazing on diatoms. Silica dissolution depends on temperature and silicic acid saturation, following the parameterization of Ridgwell et al. (2002). The last scavenging particles are lithogenic dust (dus), a nonstandard output of PISCES. Dust is deposited on the surface, sinks at a constant speed of 2 m/day, and is not remineralized. The distribution of dust deposition is based on the outputs of the Interactive with Chemistry and Aerosols atmosphere model (Hauglustaine et al., 2004), validated against atmospheric in situ and satellite data. Dust distribution in the ocean has never been validated against in situ data. As lithogenic dust is very localized, mainly in the tropical North Atlantic and in some coastal areas of the Atlantic and Indian oceans, uncertainties on its concentration little affect the determination of other K_p^ds. In PISCES, plankton does not sink; sPOC and dust sink at a constant speed of 2 m/day; bPOC, cal, and bSi sink at 50 m/day. According to Stokes' law, bPOC has to sink fast because it is large, whereas cal and bSi sink fast due to their excess density. PISCES carbon export at 100 m is 8.1 GtC/year and is the middle of the range of previous estimates.

The spatial distribution of each of the nine solid phases simulated by PISCES are shown in Figures 5 and 6. Each distribution is unique: Phytoplankton groups and microzooplankton are found only very close to the surface in the euphotic zone, whereas nonliving particles as well as mesozooplankton are found throughout the water column. Horizontally, they can be ubiquitous (phy), very localized (dus), or mainly present at high latitudes (phy2 and bSi).

Thanks to data from Lam et al. (2011) and from GEOTRACES cruises, it is known that cal and silica do not decrease fast enough with depth (see Appendix B) in the model, suggesting a too low dissolution rate. In order to estimate how much this bias could affect our ^{234}Th model, we also made simulations with corrected particle fields below 100 m, as described in Appendix B. The horizontal distribution of these two particle types is more difficult to validate because of the limited data coverage. As shown in Figure 7, PISCES cal and bSi close to the surface, including the fraction in living diatoms and coccolithophores, are often lower than
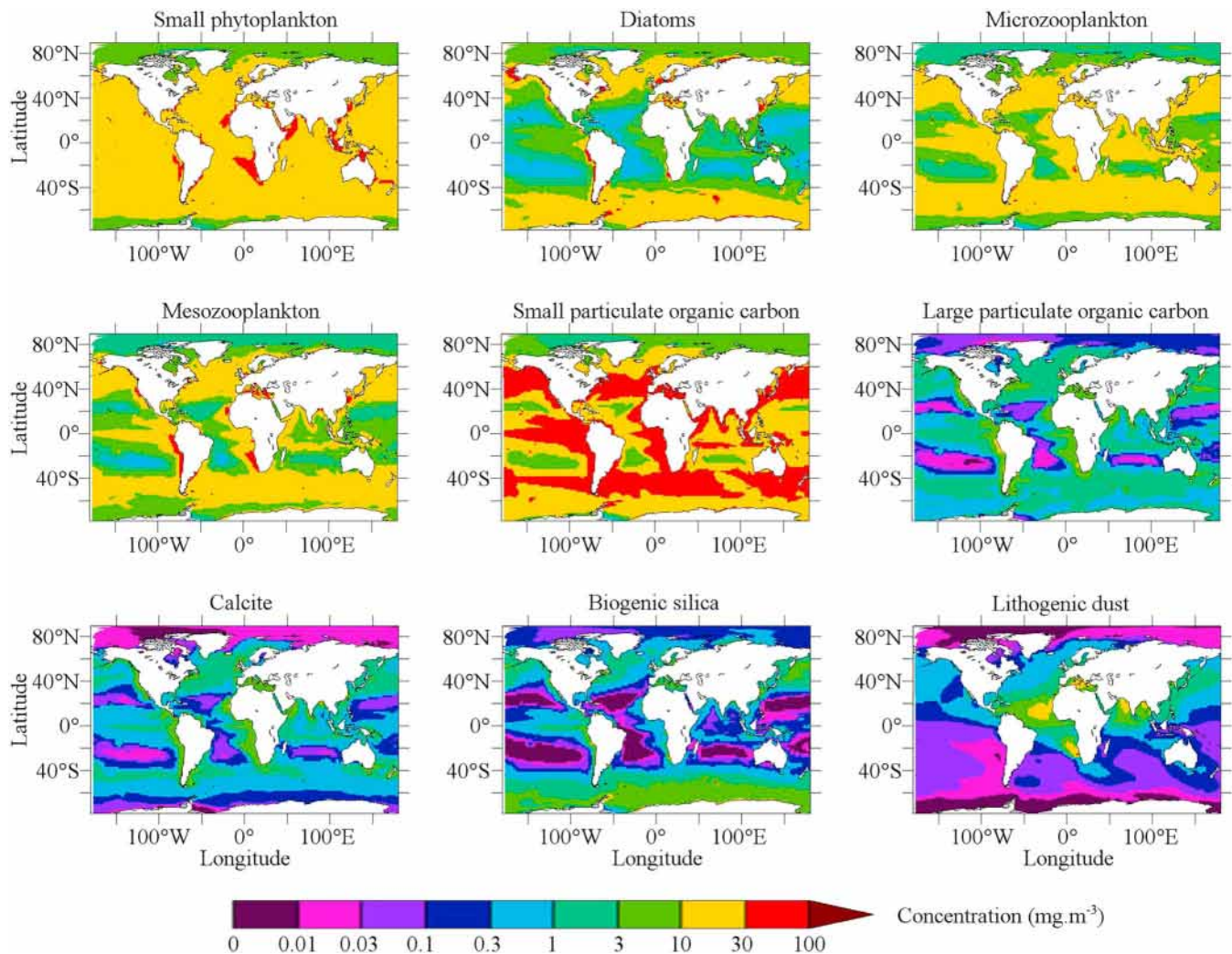
Figure 5. Particle concentrations simulated by Pelagic Interactions Scheme for Carbon and Ecosystem Studies, averaged from the surface to 100 m deep and over a year.

measured cal and bSi in regions of low productivity, particularly in the North Atlantic subtropical gyre, but tend to be higher in coastal areas.

In our model, the affinity of each particle type for ^{234}Th is defined by a partition coefficient. Scavenging processes are not explicitly represented but diagnosed from equations (6) and (7) using the concentrations and vertical speeds from PISCES. This approach greatly reduces the computational costs as only one tracer, total ^{234}Th, is transported. As the half-life of ^{234}Th is only 24.1 days, it cannot take more than 1 year to reach steady state. This is why our model simulates 2 years of ^{234}Th dynamics. What we call "model results" from now on are the ^{234}Th activities of the second year. Following Resplandy et al. (2012), we define the "equilibrium depth" as the shallowest depth at which the thorium deficit $U - Th_{tot}$ is lower than 50 dpm/m^3, and all analyses of carbon export will be performed from the surface to this depth.

2.3. Inverse Method

The goal of the inversion is to find a set of K_p^d values which makes our model results as close as possible to the observations. This is like using the model in a reverse mode, computing the unknown causal factors, that is, the partition coefficients, by using their consequences, that is, the ^{234}Th activities, justifying the adjective "inverse" for this type of method. The difference between model ^{234}Th and observations is described in the following equation:

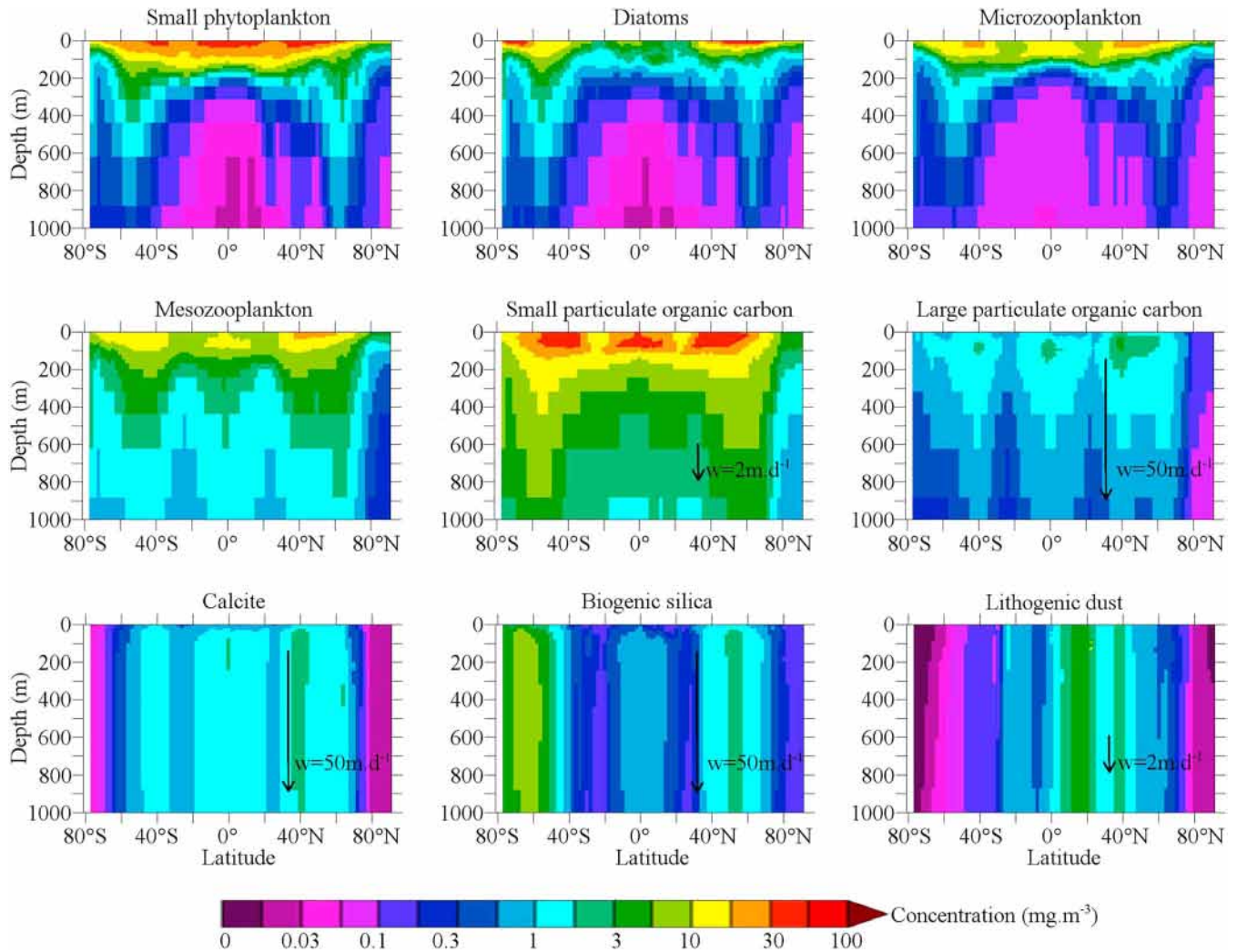$$\vec{Th}^{\,mod}(\vec{K}^d) = \vec{Th}^{\,obs} + \vec{\eta}. \tag{9}$$

Figure 6. Particle concentrations simulated by Pelagic Interactions Scheme for Carbon and Ecosystem Studies, averaged zonally and over a year.

Here $\vec{Th}^{\,\text{obs}}$ is a vector including all ^{234}Th observations, $\vec{Th}^{\,\text{mod}}$ is the vector of ^{234}Th model outputs at the same locations as in $\vec{Th}^{\,\text{obs}}$, and $\vec{\eta}$ is the vector of residuals. Inversion consists in minimizing $\vec{\eta}$ by means of an algorithm. Model ^{234}Th is taken at the horizontal grid cells and days of year of the observations. As vertical gradients are strong and can be represented by the model, model ^{234}Th is vertically interpolated at the observation depths. Since the dynamical fields used in our forward model are annual averages, interannual variations are not taken into account.

As the problem is overdetermined, with 5,361 ^{234}Th observations and 9 unknowns (the K_p^d values for each type of particle), it is impossible to exactly fit the model to the data. The optimal set of K_p^ds is found by minimizing a function of the residuals, called cost function. Two least-squares cost functions (see Appendix A) are considered: C_{tot} and C_{tp}. The first, C_{tot}, considers only the total ^{234}Th, which is the most commonly measured quantity and is used to compute carbon export in the deficit method. The second cost function, C_{tp}, also considers particulate ^{234}Th. The main advantage of C_{tp} is that particulate ^{234}Th contains information on the partition coefficients of nonsinking plankton and slowly sinking small organic particles, which together constitute the vast majority of the particulate matter but contribute little to the total ^{234}Th deficit. Model particulate ^{234}Th activity is computed using equation (7). Thus,

$$C_{\text{tot}}(\vec{K}^d) = \sum_i (Th_i^{\text{tot,mod}}(\vec{K}^d) - Th_i^{\text{tot,obs}})^2,$$ (10)
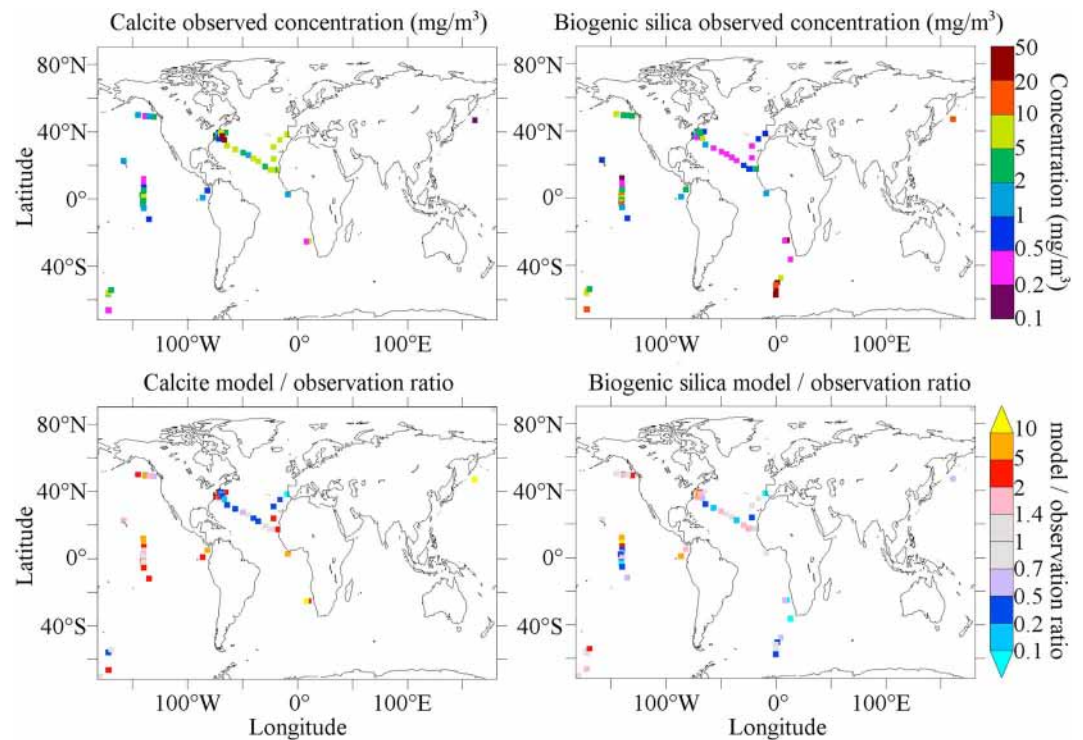
Figure 7. Observed concentrations of calcite and biogenic silica, from Lam et al. (2011) and GEOTRACES data, and comparisons with equivalent model outputs (including the detritic fraction and the fraction in living organisms).

$$C_{tp}(\vec{K}^d) = \sum_i (Th_i^{\mathrm{tot,mod}}(\vec{K}^d) - Th_i^{\mathrm{tot,obs}})^2 + \sum_j (Th_j^{\mathrm{par,mod}}(\vec{K}^d) - Th_j^{\mathrm{par,obs}})^2. \tag{11}$$

The posterior uncertainties (i.e., uncertainties in the K_p^d values) are computed by assuming that errors on observed and modeled ^{234}Th, called prior errors, have zero expectation, no correlation, and the same variance (see Appendix A). On the one hand, several reasons can make a partition coefficient highly uncertain under this approximation. If a given particle class does not adsorb much thorium, because of either a low concentration or a low partition coefficient, the relative uncertainty on its partition coefficient will be higher. The relative scarcity of observations is another source of uncertainty, particularly affecting the most localized particle types such as dust and bSi. When two particle classes have similar spatial distributions, their partition coefficients are said to be correlated (Gloor et al., 2001), increasing the uncertainties in both of them because some effects can be attributed equally to either of them. On the other hand, some types of errors are not taken into account in the estimated posterior uncertainties. Although they have a large impact on the thorium cycle, particle concentrations, vertical sinking speeds, and the oceanic circulation are not determined by the inversion but are directly taken from NEMO-PISCES. Errors in each of these physical quantities might bias the K_p^d estimates. Another neglected source of error on K_p^d values is the correlation of prior errors. Prior errors are assumed to be randomly distributed, like a white noise. If, on the contrary, they are correlated over large regions, the posterior uncertainties will be larger than estimated.

The second result of the inversion is the residuals. Residuals show what the model cannot fit. If they remain high and error variance cannot be reduced much, this would indicate that there are errors either in the observations or in the construction of the model. In an ideal case, residuals should be similar to a noise and present no coherent spatial or temporal pattern.

2.4. List of Inversions
In this study, the results of seven inversions, listed in Table 1 by increasing complexity, are presented.

The first three inversions are based on a constant K_p^d hypothesis. Their partition coefficients depend only on the nature of particles and do not vary with time and location. Adsorption dynamics is not considered: Equilibrium is assumed to be achieved immediately. The first and simplest inversion is the Control one. Control

Table 1
List of Inversions

	Control	Inv. T	Inv. TP	Inv. TZ	Inv. TPZ	Inv. TZM	Inv. TPZM
Cost function	C_{tot}	C_{tot}	C_{tp}	C_{tot}	C_{tp}	C_{tot}	C_{tot}
Particle classes	1	5	5	5	5	5	5
Sensitivity study	Yes	No	No	No	No	No	No
K^d varying with depth	No	No	No	Yes	Yes	Yes	Yes
Particle profile correction	No	No	No	No	No	Yes	Yes

uses C_{tot} as a cost function and determines only one partition coefficient, which applies to all particles. This simulation is used in two ways. First, its partition coefficient and cost functions after inversion are used as references for the other, more complex, inversions. Second, the sensitivity of the forward model to the partition coefficients is estimated around the values of the Control simulation. This step is required to decide which K_p^d can be determined by our inversions (see section 3.1). The two other inversions are T and TP. They constrain the partition coefficients of five different particle pools and differ only in the cost function they minimize: C_{tot} (T) or C_{tp} (TP).

The remaining four inversions are based on a more complex [234]Th model. They are designed to reduce the vertical biases in the residuals and to assess how assumptions on thorium cycling and biases in particle concentrations can affect our K_p^d estimates. Both the modeled and observed particle concentrations decrease with depth because of remineralization or dissolution. Remineralization and dissolution should lead to a [234]Th excess below the equilibrium depth and to low particulate [234]Th activities at depth due to the lack of particles to adsorb onto. But large excesses compared to [238]U are rarely measured, and particulate activities below the euphotic layer are relatively constant with depth, around 10% of total activities, suggesting that variations in concentrations are compensated by variations in partition coefficients. For this reason, a new degree of freedom was added in inversions TZ, TPZ, TZM, and TPZM, allowing the K_p^d of nonliving particles to vary with depth. This is a way to relax the questionable equilibrium hypothesis without suffering from the cost and complexity of an explicit dynamics model. As Th adsorption onto particles can take months (Lerner et al., 2016), it is likely that sinking particles can continue to adsorb Th on their way. Plankton does not require depth-dependent K_p^d values because it is concentrated in the euphotic layer and does not sink. This variability is implemented as a linear increase between 100 and 1,000 m.

$$K_p^d = K_{p,\text{sh}}^d \qquad (z < 100\,\text{m}). \tag{12}$$

$$K_p^d = K_{p,\text{sh}}^d + \frac{z - 100}{900}(K_{p,\text{dp}}^d - K_{p,\text{sh}}^d) \qquad (100\,\text{m} < z < 1{,}000\,\text{m}). \tag{13}$$

The subscripts sh and dp represent, respectively, shallow and deep K_p^d, which are the new parameters to estimate. The four inversions differ in the cost function they minimize and the particle fields they use. Inversions TZ and TZM minimize C_{tot}, whereas TPZ and TPZM minimize C_{tp}. Inversions TZ and TPZ use particle fields from PISCES at all depths and are directly comparable to T and TP, whereas TZM and TPZM replace PISCES particle concentrations below 100 m by a power function of depth constrained by observations, as described in Appendix B, in order to correct for known PISCES biases at these depths and assess how sensitive our inversions are to biases in particle concentrations.

In the Control inversion, the first guess for K^d is 3×10^6, which is in the middle of the wide range of previous estimates (10^4–10^9). In all other inversions, the K_p^d values are initialized from the result of Control. We have verified that our estimates did not depend on the first guess.

3. Results
3.1. Model Sensitivity and Correlation: Which Partition Coefficients Can Be Constrained?
Although the problem is formally overdetermined, it does not imply that the K_p^d value for each of the nine particle types can be determined properly by the inversion technique. Poor determination can occur if a particle type has a negligible influence on the [234]Th cycle or if it is distributed in a very similar way to another particle type. A sensitivity analysis needs to be performed to determine the K_p^d values that can be independently constrained. The sensitivities of total and particulate [234]Th activities to each of the 14 unknowns of
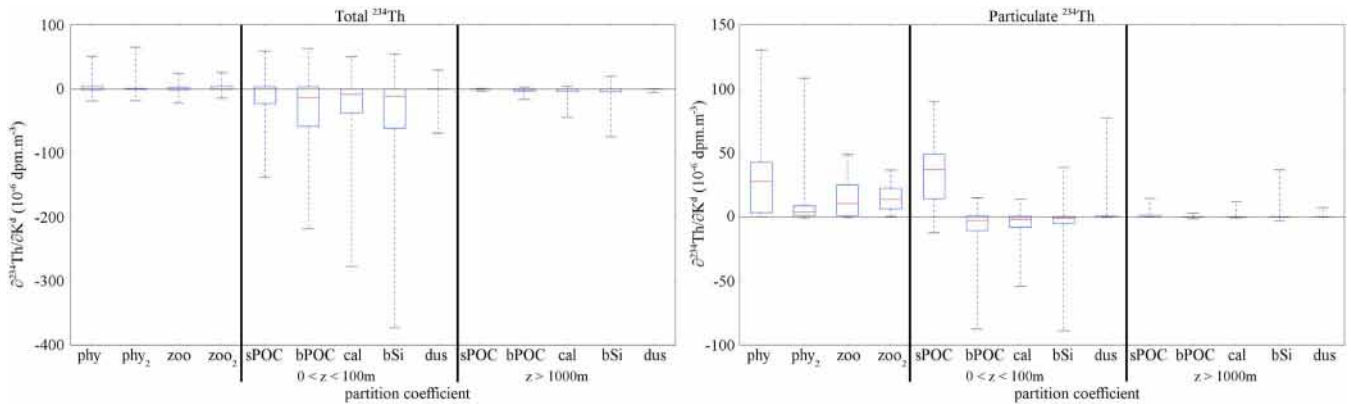
Figure 8. Sensitivity of total and particulate ^{234}Th activities to changes in the value of each partition coefficient. Boxes represent quartiles and dashed lines the whole range of values. sPOC = smaller particulate organic carbon; bPOC = larger particulate organic carbon; cal = calcite; bSi = biogenic silica; dus = dust.

our inversions have been computed. The unknowns are the partition coefficients for each of the four plankton types and two partition coefficients for each of the five other particle types: one in the upper ocean, $K^d_{p,\mathrm{sh}}$, and the other at 1,000 m deep, $K^d_{p,\mathrm{dp}}$, where p is the particle type (see section 2.4). Fourteen forward model simulations have been carried out to compute sensitivity. In each simulation, one K^d_p is increased by 0.005% compared to the standard value determined in the Control inversion. At observation point i, the model sensitivity to the partition coefficient of the particle class p at depth j (sh or dp) is

$$\sigma^i_{p,j} = \frac{\partial Th}{\partial K^d_{p,j}}. \tag{14}$$

This derivative is approximated by a forward finite difference scheme, comparing the ^{234}Th activity in the simulation with increased $K^d_{p,j}$ with the ^{234}Th activity in the Control simulation:

$$\sigma^i_{p,j} \approx \frac{Th\left(K^d_{p,j}(1+\delta)\right) - Th\left(K^d_{p,j}\right)}{\delta K^d_{p,j}}. \tag{15}$$

It has been checked that this derivative estimate was identical for any step (δ) between 0.0001% and 1%, whether the difference is forward ($\delta > 0$) or backward ($\delta < 0$). A positive (negative) sensitivity to a given K^d_p means that an increase in this K^d_p increases (decreases) the ^{234}Th activity. Particle classes with high sensitivities are likely to be important carriers (large impact on particulate ^{234}Th) or exporters (large impact on total ^{234}Th) of the trace element, unless their K^d_ps are very small. Particle classes with low sensitivities are more poorly constrained, unless they have very high K^d_ps. Indeed, they might be used by the model for second-order adjustments, potentially leading to spurious results. Sensitivity is a local quantity computed at each observation point. The total and particulate ^{234}Th sensitivities to each partition coefficient are shown in Figure 8. The ideal case to constrain a given partition coefficient is when at least some local activities are very sensitive to it, because a high sensitivity reduces the posterior uncertainty.

The 14 sensitivity simulations can also be used to compute the correlation between the impacts each K^d_p has on the ^{234}Th activities. Correlation is a global quantity that is closely related to sensitivity:

$$C_{pq} = \frac{\sum_i \sigma^i_p \sigma^i_q}{\sqrt{\sum_i \left(\sigma^i_p\right)^2 \times \sum_i \left(\sigma^i_q\right)^2}}. \tag{16}$$

Correlation between two particle classes is high (close to 1) when they have a similar distribution and role in the ^{234}Th cycle. As a consequence, the specific contribution of each of these classes may be difficult to determine, and they may need to be merged into a single pool with a single K^d_p. A negative correlation indicates particles with opposite effects on the ^{234}Th activity, which may also limit the ability of the inversion procedure to compute a precise K^d_p for these particles. In the ideal case for inversion, correlations are close
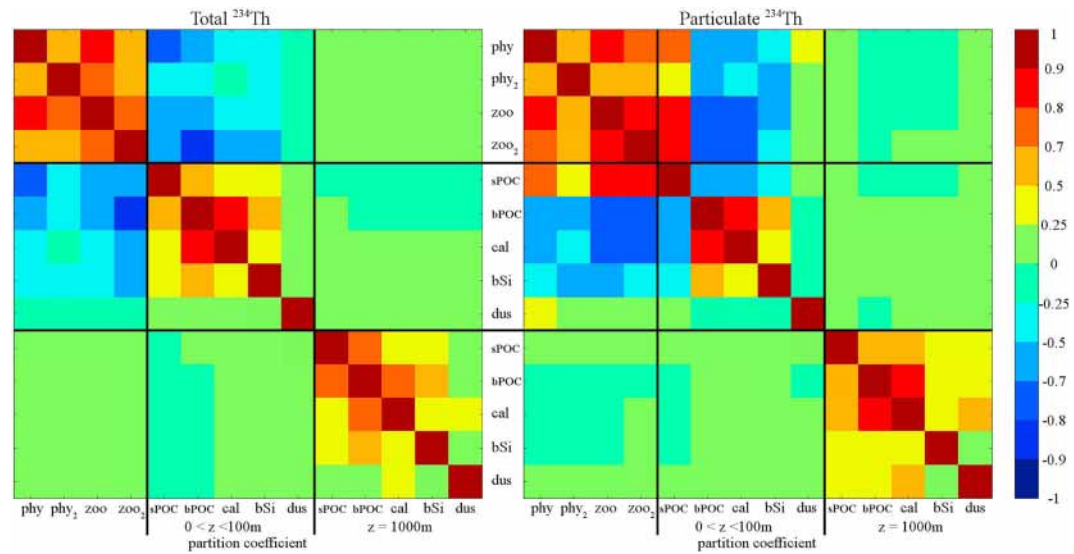
Figure 9. Correlation matrices of the sensitivity of total and particulate ^{234}Th activities to partition coefficients. sPOC = smaller particulate organic carbon; bPOC = larger particulate organic carbon; cal = calcite; bSi = biogenic silica; dus = dust.

to zero, and the various K_p^ds can be inverted separately from each others, using their own specific data. The two correlation matrices, for total and particulate ^{234}Th, are shown in Figure 9.

Total and particulate ^{234}Th (Figure 8) have very different sensitivities, meaning they contain complementary information. On the one hand, total ^{234}Th depends primarily on the K_p^ds of sinking particles in the upper 100 m. Higher values of these K_p^ds lead to a stronger export and, thus, to smaller total ^{234}Th activities in the upper ocean. Plankton has a smaller but nonnegligible impact on total ^{234}Th with an opposite sign: As plankton does not sink, the thorium adsorbed on this phase is retained in the upper ocean. On the other hand, particulate ^{234}Th is most sensitive to the most abundant particles, which are small particulate carbon and plankton. Larger K_p^d values for these particle types increase the particulate ^{234}Th activity. The effect of fast-sinking particles is far smaller, sometimes even negative because they draw down total ^{234}Th activities. Thorium-234 is less sensitive to the K_p^d of lithogenic dust, which is both far less abundant than plankton and sPOC (Figure 5) and slower to sink than bPOC, cal, and bSi. For this reason, posterior uncertainty on this K_p^d is expected to be higher. The same problem occurs with partition coefficients at 1,000 m. Particle concentrations below the euphotic layer are low, so that a large increase in deep K_p^ds has a small effect on ^{234}Th. Small observational or model errors on the deep ^{234}Th activities can largely deviate the deep K_p^ds computed by the inverse algorithm which, as a consequence, suffer from large uncertainties.

Correlation matrices of total and particulate ^{234}Th are rather similar (Figure 7). Both underline a strong correlation between the four plankton classes since none of them sinks. In PISCES, bPOC and cal are similarly distributed in space and share the same sinking speed. As a consequence, their K_p^d values are also very correlated. bSi is somewhat correlated with the other sinking particles. However, this correlation is weaker because bSi has a different distribution, with the highest concentrations found in the high latitudes (Figure 5). Dust is not correlated to the other materials because of its very specific distribution (Figure 4). The K_p^ds values at 1,000 m are relatively independent from the surface K_p^ds. sPOC exhibits very specific characteristics: Its effect on total ^{234}Th is similar to that of the other sinking particles (more deficit), whereas its effect on particulate ^{234}Th looks like that of nonsinking plankton (more particulate ^{234}Th).

Three consequences arise from these results. First, total and particulate ^{234}Th contain complementary information. Adding particulate thorium in the cost function makes it possible to better constrain the partition coefficients of plankton and sPOC. Second, some K_p^d values cannot be determined individually. The four plankton types do not have distinct enough signatures to be considered separately. Thus, in the rest of this study, all plankton types are merged into a single pool with a unique K^d. For the same reason, bPOC and cal are also merged. All other K_p^d values are determined individually. Finally, the K_p^ds of all particle types at 1,000 m and of lithogenic dust at surface are expected to suffer from large uncertainties. However, esti-

Table 2
Partition Coefficients After Each Inversion, Plus or Minus One Standard Deviation

Inversion	Cost function	Profile correction	Depth level	K_p^d (10^6)				
				Plankton	sPOC	bPOC/cal	bSi	dust
Control	C_{tot}	No	All			1.95–2.02		
T	C_{tot}	No	All	7.51–9.05	8.36–9.66	2.14–2.33	1.10–1.29	10.8–15.5
TP	C_{tp}	No	All	1.80–2.07	3.93–4.32	1.90–2.03	1.29–1.44	14.0–16.7
TZ	C_{tot}	No	z < 100 m	5.32–6.66	8.45–9.66	1.89–2.07	0.79–0.99	7.4–11.7
			z = 1,000 m		48.7–78.9	7.35–9.50	0.26–1.74	82–187
TPZ	C_{tp}	No	z < 100 m	1.42–1.69	4.39–4.79	1.81–1.94	1.06–1.21	12.5–15.0
			z = 1,000 m		16.5–26.1	8.8–10.5	0.70–1.90	59–115
TZM	C_{tot}	Yes	z < 100 m	5.55–6.91	9.7–11.0	1.71–1.89	0.79–1.01	6.1–10.3
			z = 1,000 m		60.2–89.2	11.4–15.6	4.38–9.00	57–167
TPZM	C_{tp}	Yes	z < 100 m	1.26–1.53	4.73–5.14	1.70–1.84	1.07–1.23	12.0–14.5
			z = 1,000 m		10.8–17.5	18.0–20.9	8.1–11.4	49–107

Note. sPOC = smaller particulate organic carbon; bPOC = larger particulate organic carbon; cal = calcite; bSi = biogenic silica.

mating them should not have detrimental effects on the determinations of the other K^ds because they are controlled by different subsets of the observations.

3.2. Partition Coefficients and Residuals After Inversion

Inversions T and TP produced a K_p^d estimate for each of the five following particle types: plankton, sPOC, bPOC/cal, bSi, and lithogenic dust (see Table 2). These partition coefficients are constant both in space and time. They differ between the two inversions because they are based on two different cost functions. The five K_p^d estimates are displayed in Table 2 with confidence intervals based on one standard deviation. The residuals of TP are shown in Figure 10. Positive residuals indicate that the model overestimates ^{234}Th activity. In the case of total ^{234}Th, this means that export is underestimated, whereas in the case of particulate ^{234}Th, it means that the affinity of particles for ^{234}Th is overestimated.

The partition coefficient estimated in the Control inversion is $1.95 - 2.02 \times 10^6$. The K_p^d values estimated by inversions T and TP range between 1.1×10^6 and 16.7×10^6, confirming that thorium is a highly particle-reactive element. Two main results are established: bSi has a lower affinity for thorium than the other phases, and small particles have a higher affinity than large particles. The K_p^d estimates of the fast-sinking particles are not very sensitive to the choice of the cost function. This result is consistent with our sensitivity analysis: These particles have a large impact on the total ^{234}Th deficit but a small impact on particulate ^{234}Th activities. The K_p^d for bPOC and cal is $1.90 - 2.33 \times 10^6$, whereas the K_p^d for bSi is $1.10 - 1.44 \times 10^6$, about 40% lower. Plankton and slowly sinking particles have higher K_p^ds, but their values depend on the chosen cost function. Lithogenic dust has the highest K_p^d, between 10.8 and 16.7×10^6. The K_p^d values of sPOC and plankton produced by inversion T display much higher values ($8.28 - 9.58 \times 10^6$ and $7.87 - 9.45 \times 10^6$, respectively) than those obtained with inversion TP ($3.85 - 4.24 \times 10^6$ and $1.83 - 2.09 \times 10^6$). As explained in section 3.1, particulate ^{234}Th is more sensitive to these two partition coefficients than total ^{234}Th, making the results of inversion TP more reliable than those of T.

With the K_p^d estimates from inversion TP, 30.6% of ^{234}Th sinking below the equilibrium depth is exported by sPOC, 25.8% by bPOC, 20.4% by cal, 16.4% by bSi, and 6.8% by dust. As a consequence of their higher K_p^ds and concentrations, sPOC and dust drive 37.4% of the total thorium export, despite having a much slower sinking speed. Down to the equilibrium depth, the global average total ^{234}Th activity is 2,141 dpm/m^3, 17.1% of which is attached to particles. Most of this particulate ^{234}Th is carried by slow or nonsinking particles: 41.8% is carried by plankton, 48.4% by sPOC, and 7.0% by lithogenic dust but only 1.2% by bPOC, 0.9% by cal, and 0.7% by bSi.

The residuals constitute another very important source of information in inversions. The root mean square error (rmse), a proxy of the cost function representing the average distance between the model and the observations, remains high (see Table 3). The standard deviation computed from the observations of total ^{234}Th is 456.8 dpm/m^3. The root mean square of the residuals after the Control inversion is 22% lower, 356.4
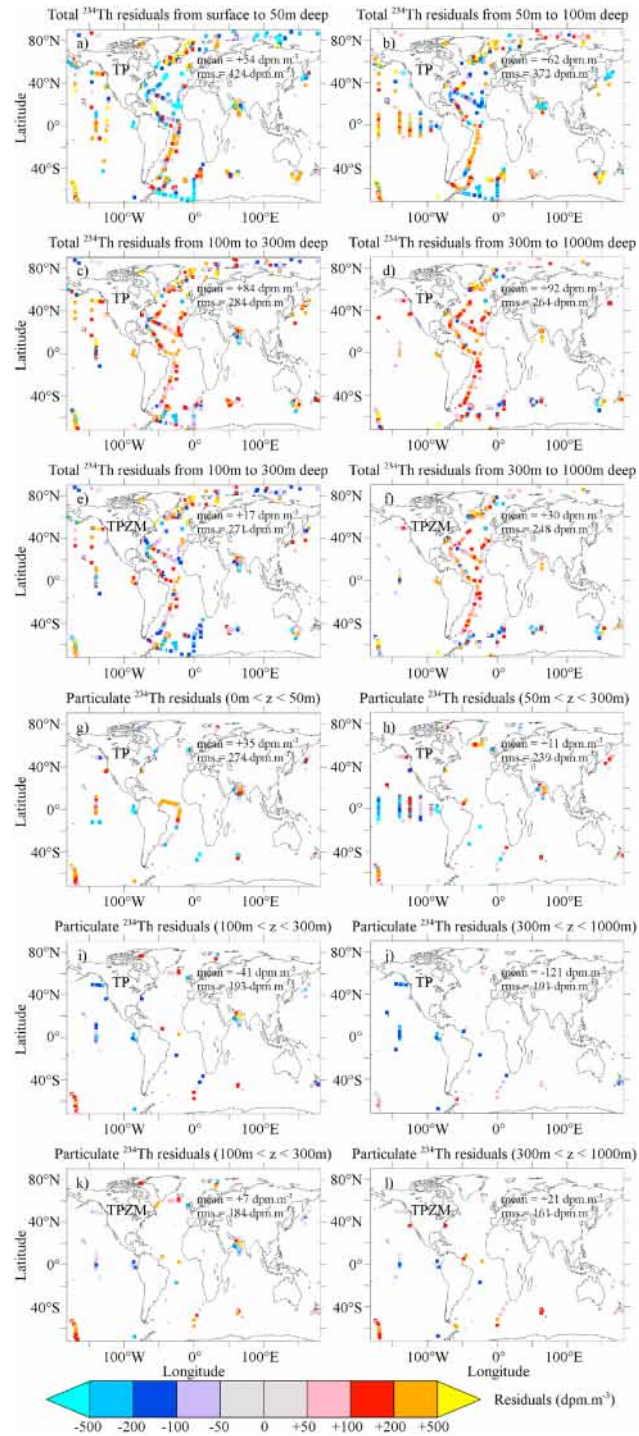
Figure 10. Total (from a to f) and particulate (g to l) [234]Th residuals after inversion at different depths. The cost function is C_{tp}. Residuals after inversion TP are shown for all depths (a–d, g–j). Residuals after inversion TPZM (using depth-variable partition coefficients and profile correction) are shown for depths greater than 100 m (e, f, k, l).

Table 3
Mean and Root Mean Square (rms) Residuals of Total and Particulate ^{234}Th After Each Inversion

Inversion	Cost function	Profile correction	Depth level	Mean (dpm/m^3) total	Mean (dpm/m^3) particulate	rms (dpm/m^3) total	rms (dpm/m^3) particulate
Control	C_{tot}	No	z < 100 m	+82.7	−93.8	418.3	281.2
			100 m < z < 1,000 m	+67.9	−145.5	273.5	224.1
			All	+75.6	−113.9	356.4	260.5
T	C_{tot}	No	z < 100 m	+47.5	+439.6	396.7	525.7
			100 m < z < 1,000 m	+77.3	+147.2	277.1	297.6
			All	+61.8	+325.9	344.7	451.0
TP	C_{tp}	No	z < 100 m	+57.5	+20.7	403.0	255.0
			100 m < z < 1,000 m	+86.8	−63.5	277.3	192.4
			All	+71.6	−12.0	348.5	232.7
TZ	C_{tot}	No	z < 100 m	+51.3	+354.9	393.3	456.1
			100 m < z < 1,000 m	+7.2	+212.1	267.4	318.6
			All	+30.2	+299.4	338.9	408.2
TPZ	C_{tp}	No	z < 100 m	+62.4	+9.2	400.0	254.4
			100 m < z < 1,000 m	+14.4	−15.9	265.5	186.4
			All	+39.4	−0.6	342.2	230.4
TZM	C_{tot}	Yes	z < 100 m	+49.2	+385.8	392.6	482.7
			100 m < z < 1,000 m	+11.0	+344.4	262.7	413.6
			All	+30.9	+369.7	336.7	457.1
TPZM	C_{tp}	Yes	z < 100 m	+63.6	+9.1	399.6	254.5
			100 m < z < 1,000 m	+21.0	+10.6	263.7	177.8
			All	+43.2	+9.7	341.3	227.8

dpm/m^3. In the case of inversion T, it is equal to 344.7 dpm/m^3 (or 43% of explained variance), which is not a large gain compared to the Control experiment. Control and T inversions, using C_{tot} as a cost function, poorly reproduce particulate ^{234}Th. In Control, the single K_p^d largely represents the small K_p^d of large particles responsible for the majority of particle export and cannot account for all the particle-bound ^{234}Th. In T, the K_p^d of small particles is much larger than that of large particles, in order to account for the observed ^{234}Th deficit in low productivity areas, but this change leads to unrealistically high particulate ^{234}Th activities. In inversion TP, using C_{tp} as a cost function drastically reduces the overall bias on particulate ^{234}Th and divides its rmse by two, as the cost of a very small increase in the rmse of total ^{234}Th (+3.8 dpm/m^3). Thus, a lot of additional information, especially on small particles, can be extracted from particulate ^{234}Th at the cost of only a slight reduction in the ability of the model to represent total ^{234}Th deficit.

Inspection of the residuals also reveals some systematic biases. For instance, in the eastern equatorial Pacific, ^{234}Th observations between 20° N, 20° S, 95° W, and 170° W are relatively homogeneous, but the inversion reveals negative residuals close to the western coast of America and positive residuals more offshore. This result suggests that, in the model, scavenging decreases too quickly toward the open ocean, which might be related to the particle fields of PISCES. Another pattern in the residuals is seen in the high latitudes, where the total ^{234}Th activities, generally measured in late summer, tend to be underestimated by the model, whereas the spring and early summer activities tend to be overestimated. In the South Atlantic subtropical gyre, the total ^{234}Th observations acquired during GEOTRACES GA02 exhibit neither very low nor very high values, which suggests moderate scavenging. Yet the model predicts almost no scavenging as a result of very low simulated concentrations of sinking particles in this region. As a consequence, the total ^{234}Th residuals are systematically positive.

The largest biases in the inversion are found in the vertical distribution of ^{234}Th activities, as indicated by the mean residuals in Table 2. At low and middle latitudes, deeper than 100 m, inversion TP portrays higher total ^{234}Th and lower particulate ^{234}Th activities than in the observations (Table 3). On average, between 300 and 1,000 m, particulate ^{234}Th is more than twice as high in the observations as in the model. At these

depths, the model after inversion presents a total ^{234}Th excess due to the release of thorium by particles when they are remineralized or dissolved. Such an excess is sometimes present in the observations, but it is not systematic and remains small. This bias in our model does not occur in the high latitudes because of the large and deep vertical mixing in winter. Since particles produced in the surface have time to scavenge more trace metals during their descent, the partition coefficients could increase with depth. This option would bring a solution to the bias diagnosed for the deep ^{234}Th excess, as it compensates for the loss of particulate matter and maintains the same vertical thorium flux. Such a modification can be implemented without changing the physical and biogeochemical models and is presented in the next section.

3.3. Inversions With Depth-Dependent Partition Coefficients

Our sensitivity experiments have shown that nine partition coefficients can be determined by inversions TZ and TPZ (see section 3.1): one for plankton and two for each of the four sinking particle classes (sPOC, bPOC and cal, bSi, and dust). Each sinking particle class can be characterized by a K_p^d between the surface and 100 m and another K_p^d at a depth of 1,000 m. Partition coefficients are set to vary between 100 and 1,000 m in a linear way (cf. equations (12) and (13)). The resulting K_p^d estimates are shown in Table 2. Surface K_p^d values are very similar to the depth-invariant K_p^ds of inversions T and TP. This is because the inversion is most sensitive to ^{234}Th activities in the mixed layer (see Figure 8), where most of the deficit occurs. Because of lower sensitivities at greater depths, K_p^ds at 1,000 m have higher uncertainties, even in relative terms. As expected, deep K_p^ds are much higher than surface ones, usually by one order of magnitude. They range from 0.26×10^6 to 187×10^6. Only bSi has a K_p^d of the same order of magnitude throughout the water column.

This peculiar behavior of bSi is linked to the lack of significant vertical variations in bSi in PISCES, as shown in Figure 6. As sinking bSi is dissolved very slowly in the model, it does not release much thorium below the euphotic layer and cannot create a ^{234}Th excess. A vertically uniform K^d is then able to account for the deep near equilibrium, and no increase with depth is required. However, this feature is likely to be spurious. In situ data from GEOTRACES and from Lam et al. (2011) exhibit a significant decrease in bSi with depth. Other particle pools of PISCES are also shown to have some bias. In particular, simulated vertical profiles of cal show the same deficiency as bSi: Cal is dissolved far too slowly in the model. In order to correct for these biases, particle concentrations deeper than 100 m are replaced in the last two inversions by data-constrained distributions, described in Appendix B.

Inversions TZM and TPZM only differ from TZ and TPZ by the profile correction scheme. Unsurprisingly, TZM and TPZM produce surface K_p^ds similar to that of the other inversions (Table 2). As the concentration of dust is unchanged and the concentration of small particulate organic carbon is only modestly altered, the deep K_p^d values of these two particle classes in deep waters are also little changed in TZM and TPZM in comparison with TZ and TPZ, respectively (the confidence intervals overlap). The major changes produced by TZM and TPZM are an increase by a factor of 2 in the deep K_p^d of bPOC and cal and by a factor of 6 to 8 for the K_p^d of bSi, making the deep K_p^ds more similar to each other. In TZM and TPZM, all partition coefficients in deep waters are larger than 4.38×10^6 and are between 3 and 14 times as high as the surface partition coefficients.

Inversions with depth-dependent partition coefficients reduce the residuals but only by a limited amount (see Table 3). The rmse for both total and particulate ^{234}Th are reduced by less than 2% when depth-dependent K_p^d is allowed. Only 4% to 5% of the error variance in T and TP inversions can be explained by allowing K_p^d to grow linearly with depth. This figure is higher for data below 100 m but still quite low: around 10% of total ^{234}Th and 15% of particulate ^{234}Th error variance. This modest gain can be explained by the predominance of noise-like errors and the existence of other biases. The effect of depth-dependent K_p^d is better highlighted by the map of the residuals from TPZM between 100 and 1,000 m (Figures 10e, 10f, 10k, and 10l), which should be compared with the same map for TP (Figures 10c,10d, 10i, and 10j). The total ^{234}Th residuals from TPZM and TP display very similar spatial patterns, as overestimates and underestimates occur at the same locations and have the same orders of magnitude. However, the average bias is divided by five between 100 and 300 m and by three below 300 m. Particulate ^{234}Th bias was divided by six, and its sign reversed from an underestimation to a slight overestimation. As the standard deviation of the residuals is one order of magnitude larger than their mean, the change is little visible on the maps of the residuals. The model after inversion is no longer systematically overestimating ^{234}Th activities below the euphotic layer due to a lack of scavenging. This improvement depends little on the particle distribution used as evidenced by the absence of notable changes in variances and biases between TPZ and TPZM. Indeed, scavenging
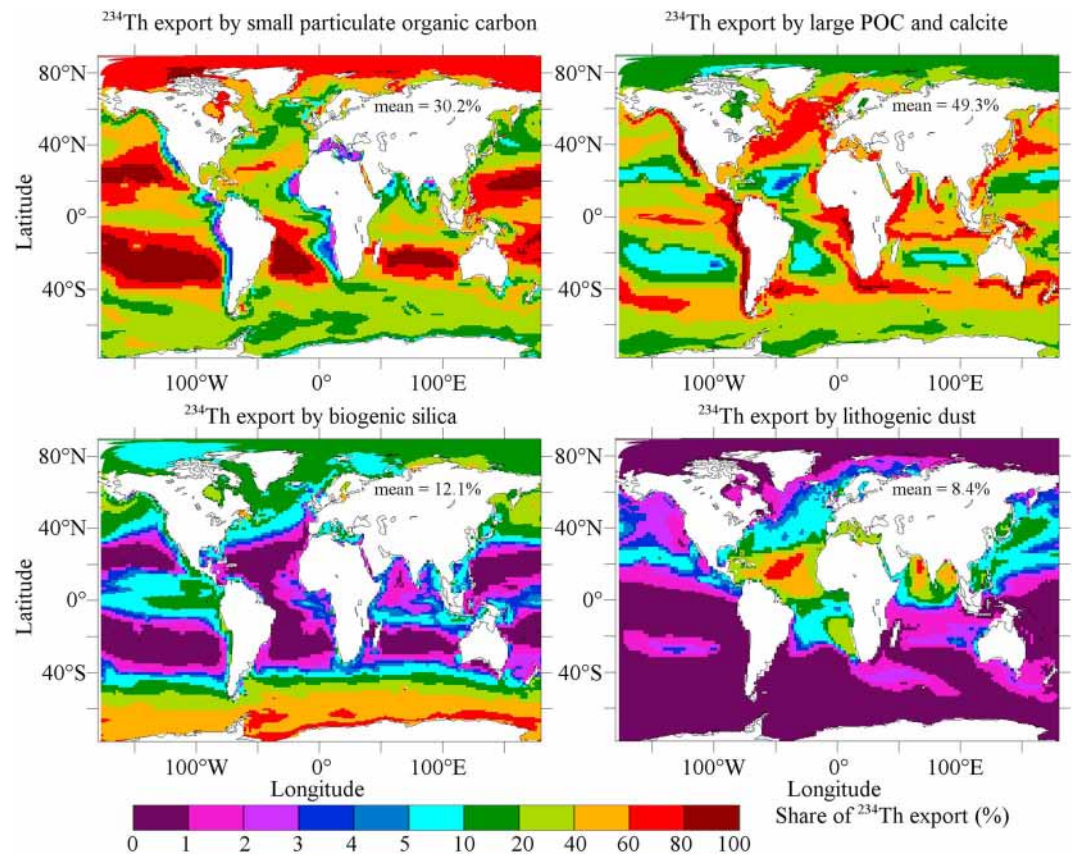
Figure 11. Contribution of each particle class to ^{234}Th export at the equilibrium depth, averaged over 1 year (inversion TPZM).

depends on the product $K_p^d C_p$, not directly on K_p^d. This means that a change in the particle concentrations changes the partition coefficients but does not necessarily change the modeled ^{234}Th activities.

Results from inversion TPZM suggest that each particle type is a major ^{234}Th scavenger in at least some regions of the world ocean (Figure 11). Lithogenic dust explains about 50% of the export at the equilibrium depth in the low latitudes of the North Atlantic and Indian Oceans. In the rest of the ocean, they play a negligible role in ^{234}Th export. bSi is the largest cause of export in the Southern Ocean. At the global scale, lithogenic dust only accounts for 8.4% of the ^{234}Th export and bSi for 12.1%. sPOC, bPOC, and cal are the largest contributors to ^{234}Th export globally, with 30.2% for sPOC, 23.4% for bPOC, and 25.9% for cal. sPOC dominates in the oligotrophic gyres, whereas bPOC and cal dominate in productive regions such as the eastern boundary upwelling systems. The one-box carbon export models usually rely on the assumption that the average carbon to ^{234}Th ratio for sinking particles is equal to the equivalent ratio for the large sinking particles. Yet our model suggests that this assumption may not hold as the contribution from small materials, whose partition coefficients are much larger, may be far from small: For instance, in the subtropical gyres, small particles contribute to more than 90% to ^{234}Th export.

4. Discussion

4.1. Comparisons With Other Partition Coefficient Estimates
The partition coefficients of thorium isotopes for particles reported in previous studies lie between 10^4 (Lin et al., 2015) and 10^9 (Dutay et al., 2009; Hayes et al., 2015), which is a very large range. Furthermore, studies tend to disagree on the major carrier phases of Th in ocean waters. Our novel approach, based on a global inversion with a 3-D time-dependent model, sheds a new light to this issue.

It has already been proposed that bSi was not a major carrier phase of thorium. From an analysis of sediment trap particles, Chase et al. (2002) has shown that the K^d of ^{230}Th was one order of magnitude lower in regions where silica was the most common particulate matter. However, such a result has not been shown to hold

for ^{234}Th. In our study, the partition coefficient for bSi is, at all depths, twice smaller than the partition coefficient for large POC and cal and up to 10 times smaller compared to that for small particles, suggesting the same pattern also exists for ^{234}Th.

Variation in K_p^d with size is a more controversial issue. As most aerosols are smaller than 20 µm (Mahowald et al., 2014), lithogenic dust should be considered as small particles. Small particles have high surface to volume ratios and would therefore be good sorbents of dissolved metals. Furthermore, according to Stokes' law, small particles should sink slower and spend more time in the upper layer, increasing their scavenging ability. This expectation is not always confirmed by observations. In situ measurements are contradictory on this point, as some of them show a higher K_p^d for particles larger than 53 µm (Buesseler et al., 1995; Moran et al., 2003). The fractal nature of aggregates is a possible explanation for the lack of a clear relationship between K_p^d and particle size (Burd et al., 2007): If mass is not proportional to the third power of particle radius but varies more slowly, then the surface to volume ratio of particles does not necessarily decrease with size. According to Burd et al. (2007), the fractal dimension of particles varies between 1.26 and 2.6. Another possibility is that thorium is adsorbed by colloids and brought to larger particles by aggregation (Honeyman & Santschi, 1989), in which case, partition coefficients should not depend much on size. Burd et al. (2000) proposed an adsorption-aggregation model where colloids have a smaller K_p^d but small (0.5–53 µm) and large (>53 µm) particles have the same K_p^d.

Decrease in the particulate C:^{234}Th ratio (and thus increase in K^d) with depth is a common feature to most data profiles used in this study. This is why allowing the model partition coefficients to increase with depth is decisive in correcting the lack of particulate ^{234}Th between 100 and 1,000 m deep in the model compared to observations. The increase of K_p^d with depth is necessary to maintain the relatively constant observed rate of 10% particulate ^{234}Th below the euphotic layer, in spite of particle concentrations decreasing with depth. Interestingly, this result can be explained with a full adsorption/desorption dynamics. Using a scavenging model not assuming instantaneous equilibrium, Lerner et al. (2017) estimated apparent first-order rate constants of Th adsorption (k_1), Th desorption (k_{-1}), and particle degradation (β_{-1}) at 11 stations of the U.S. GEOTRACES North Atlantic Section (GA03) by inverse modeling. They showed that the ratio $k_1/(k_{-1} + \beta_{-1})$, normalized to bulk particle concentration, was in the range $2–4 \times 10^7$ and did not vary systematically with depth. This ratio represents the equilibrium partition coefficient of a long-lived thorium isotope, such as ^{230}Th. As radioactive decay is a larger sink of particulate ^{234}Th than desorption or remineralization, the equilibrium partition coefficient of this isotope should be lower, around 5×10^6, to be considered as an average for all size and chemistry classes. As desorption is slower than radioactive decay (Murnane et al., 1994), the time to reach equilibrium is in the order of a few half-lives or around 1 or 2 months. In this amount of time, fast-sinking particles can sink by more than 1,000 m and continue to scavenge thorium on their way, explaining why their K_p^ds increase in a near-linear way with depth. However, this mechanism poorly explains why the K_p^d of small particles also increases with depth in our inversions. Since small particles have a vertical speed of only 2 m/day in our model, they should already be very close to equilibrium after sinking by 100 m. But size-fractionated observations of the C:^{234}Th ratio, when available, confirm our results. For instance, Planchon et al. (2013) showed that the C:^{234}Th ratio of small particles in the Southern Ocean decreased with depth down to 500 m in the same way as that of large particles. Since the sPOC reaching this depth is likely to be the most refractory fraction, it does not have the same chemical properties than the more labile surface sPOC. Preferential remineralization of carbon over thorium or a change in surface ligands could explain the increase in K_p^d, as already suggested by Buesseler et al. (2006).

In reality, particles often are aggregates containing several types of material. For instance, cal and silica have an organic coating (Decho, 1990; Passow, 2002). Lin et al. (2015) found that pure mineral nanoparticles (20 nm) and metal oxides had a low affinity for ^{234}Th, with K_p^d values between $10^{4.4}$ and $10^{5.6}$. However, with an organic coating, partition coefficients were found to lie between $10^{6.6}$ and $10^{7.8}$, two orders of magnitude larger. Even the K_p^d for silica can reach $10^{7.7}$. This is close to the value found for acid polysaccharides by Santschi et al. (2006). The K_p^d values for particles coated with organic material were found to be closer to our K_p^d for silica (10^6 in surface waters and 10^7 in deep waters) and dust (10^7 in surface waters and 10^8 in deep waters), although the natural particles we consider are much larger in size than colloids. The K_p^d values inferred here by inversion for silica (or any other phase) is then likely not to apply to pure silica but rather to natural silica-rich particles, which incidentally contain other elements and several organic compounds.
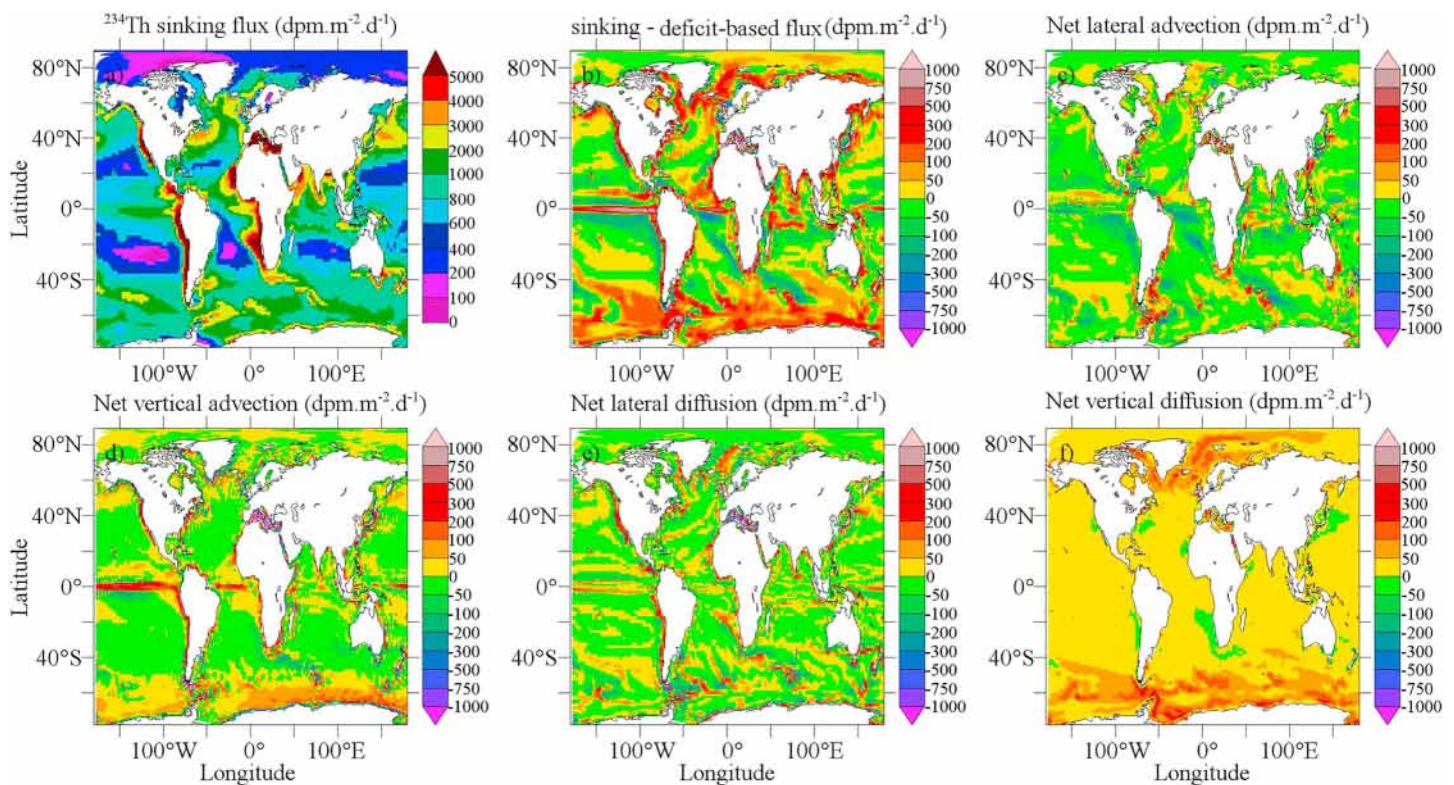
Figure 12. Map of the model ^{234}Th sinking flux at the equilibrium depth (a), error made by 1-D deficit-based estimates when neglecting transport by the oceanic circulation (b), and contributions of four transport components (c–f) to this error averaged over a year. The partition coefficients after inversion TPZM are used in this simulation.

4.2. Evaluation of 1-D ^{234}Th-Based Carbon Export Models

Although our inversion does not constrain carbon fluxes, it does provide useful information on the use of ^{234}Th as a proxy of ocean carbon export. Several assumptions made in most one-box carbon export models are debatable: ^{234}Th is assumed to be exported by large particles only; ^{234}Th activities are assumed to be at steady state and negligibly influenced by transport. In our model, these assumptions do not generally hold.

Carbon export models require a C:^{234}Th ratio of particles to convert a ^{234}Th flux into a carbon flux. All methods to estimate this ratio have limitations. Burd et al. (2007) noticed that using pumps produces a C:^{234}Th ratio representative of the most common particles, whereas the required C:^{234}Th ratio must be representative of thorium scavenging particles and weighted by sinking speeds. Small particles are the most common, but they sink much more slowly than larger ones. This is why the C:^{234}Th ratio is generally not computed on all particles but only on particles larger than 53 µm, assumed to represent most of the sinking material. However, recent studies based on in situ data and inverse methods challenge this assumption. For instance, according to Richardson and Jackson (2007) and Stukel and Landry (2010), small phytoplankton contribute to carbon export proportionally to its net primary production. Puigcorbé et al. (2015) argue that particles smaller than 53 µm might represent up to 50% of total carbon export and that multiple particle size class sampling are required when using the ^{234}Th:^{238}U method. In PISCES, small particles represent 30.8% of total export, but in our inversion, due to their higher partition coefficients, they represent an even higher proportion of ^{234}Th export, 38.6% as a global average and up to 90% in some regions, such as the subtropical gyres. In these regions, our model suggests that using the larger C:^{234}Th ratio of large particles instead of that of small particles leads to overestimating the carbon fluxes by as much as 100%. Sediment traps are less affected than pumps by this design since by conception, they collect sinking particles. But they are harder to deploy than pumps, and up to now, they have been less often used to determine C:^{234}Th ratios (Le Moigne et al., 2013).

The yearly averaged contributions of each component of transport to the ^{234}Th deficit above the equilibrium depth are shown in Figure 12. Together, the horizontal and vertical components of advection and diffusion
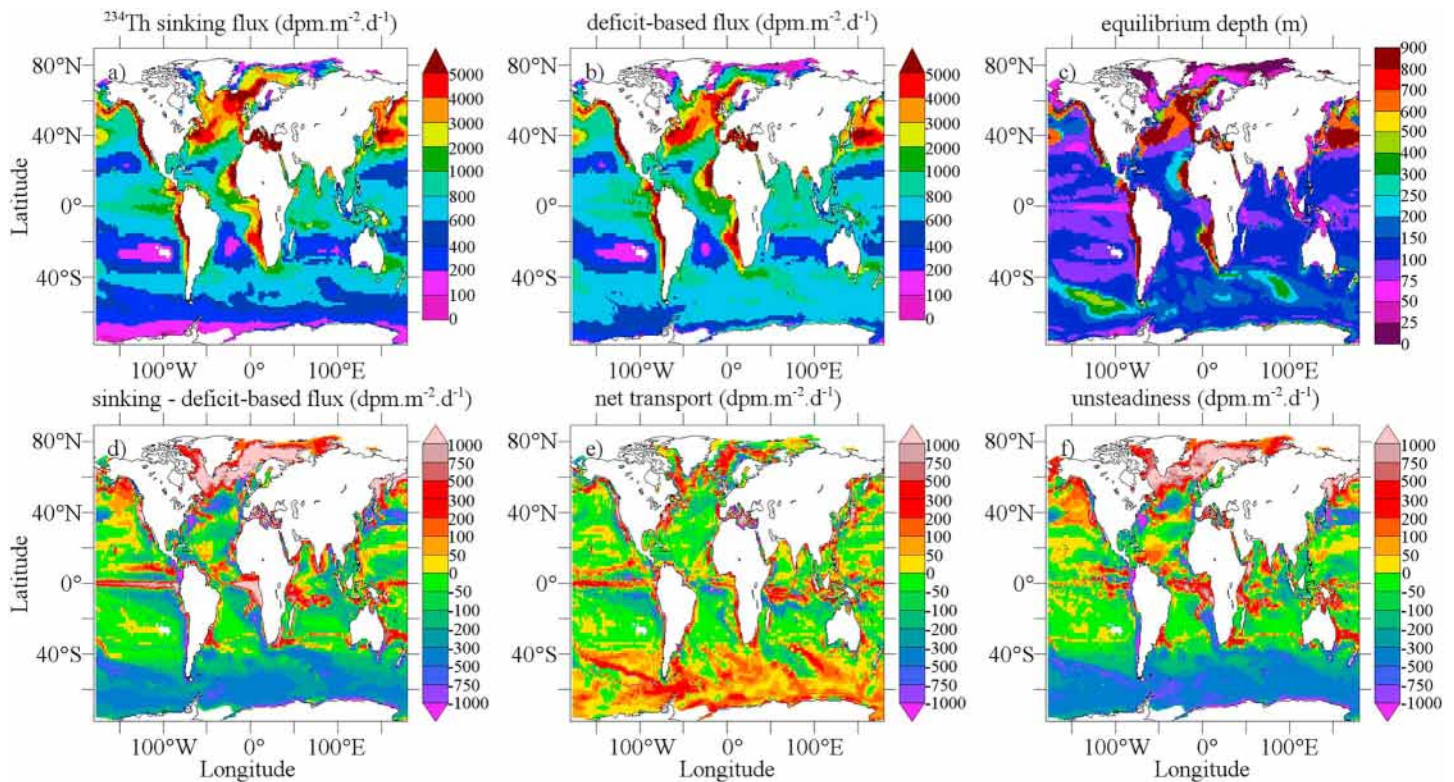
Figure 13. Model ^{234}Th sinking flux (a), 1-D deficit-based estimates (b), and their differences (d) at the equilibrium depth (c) at the solstice of June. The difference is caused by transport (e) and unsteadiness (f). The partition coefficients after inversion TPZM are used in this simulation.

(Figures 12c–12f) explain most of the difference (Figure 12b) between the model ^{234}Th sinking flux and the flux estimated using equation (3) and our model ^{234}Th activity outputs. None of the contributions is completely negligible. Vertical diffusion is particularly important at high latitudes and replenishes the mixed layer with ^{234}Th. On average, advection and diffusion create a ^{234}Th flux from deep to surface waters, reducing ^{234}Th deficit by a small amount (3%). However, at high latitudes or in equatorial upwellings, transport often modifies the ^{234}Th deficit by more than 10%. Export at equilibrium depth is then underestimated in the same proportion by assuming that scavenging is only balanced by ^{234}Th production through ^{238}U decay.

Annual averages can be misleading, especially at high latitudes, since scavenging and transport are seasonal processes. Figures 13 and 14 represent the errors in ^{234}Th export made by assuming steady state and neglecting transport at a specific date. The two dates chosen are the solstices of June and December, because they are periods when the time variability is particularly high in our model. The nonsteady-state term is computed using a time interval of 20 days around the corresponding solstice. This is similar to nonsteady-state models whose time intervals vary between 10 days and 2 months (Le Moigne et al., 2013). At high latitudes at the beginning of summer (June in the Northern Hemisphere and December in the Southern Hemisphere), ^{234}Th is being scavenged, but its activity remains high. Steady-state one-box models underestimate scavenging for two reasons: They do not see that ^{234}Th activities are decreasing and that net transport reduces the deficit. This result is significant because a lot of ^{234}Th studies are performed in spring and early summer, when ^{234}Th activity is likely to be decreasing. Nonsteady-state one-box models correct the first error but still underestimate thorium export because they neglect transport. At 60° N in the North Atlantic in June or 60° S in December, sinking fluxes are typically between 2,000 and 5,000 dpm·m^{-2}·day^{-1}, but in our simulation based on inversion TPZM, steady-state one-box models often underestimate them by more than 1,000 dpm·m^{-2}·day^{-1}. The time when the bias is largest depends on year and location: It is generally the beginning of the phytoplankton bloom, when scavenging is high and the ^{234}Th deficit is still low. Errors of the opposite sign, that is, carbon fluxes overestimations, can occur during post-bloom periods, later in summer (not shown), when particle concentration is low but the large deficit established during the previous weeks is still present, although at high latitudes, vertical diffusion alleviates overestimation. In low latitude upwelling
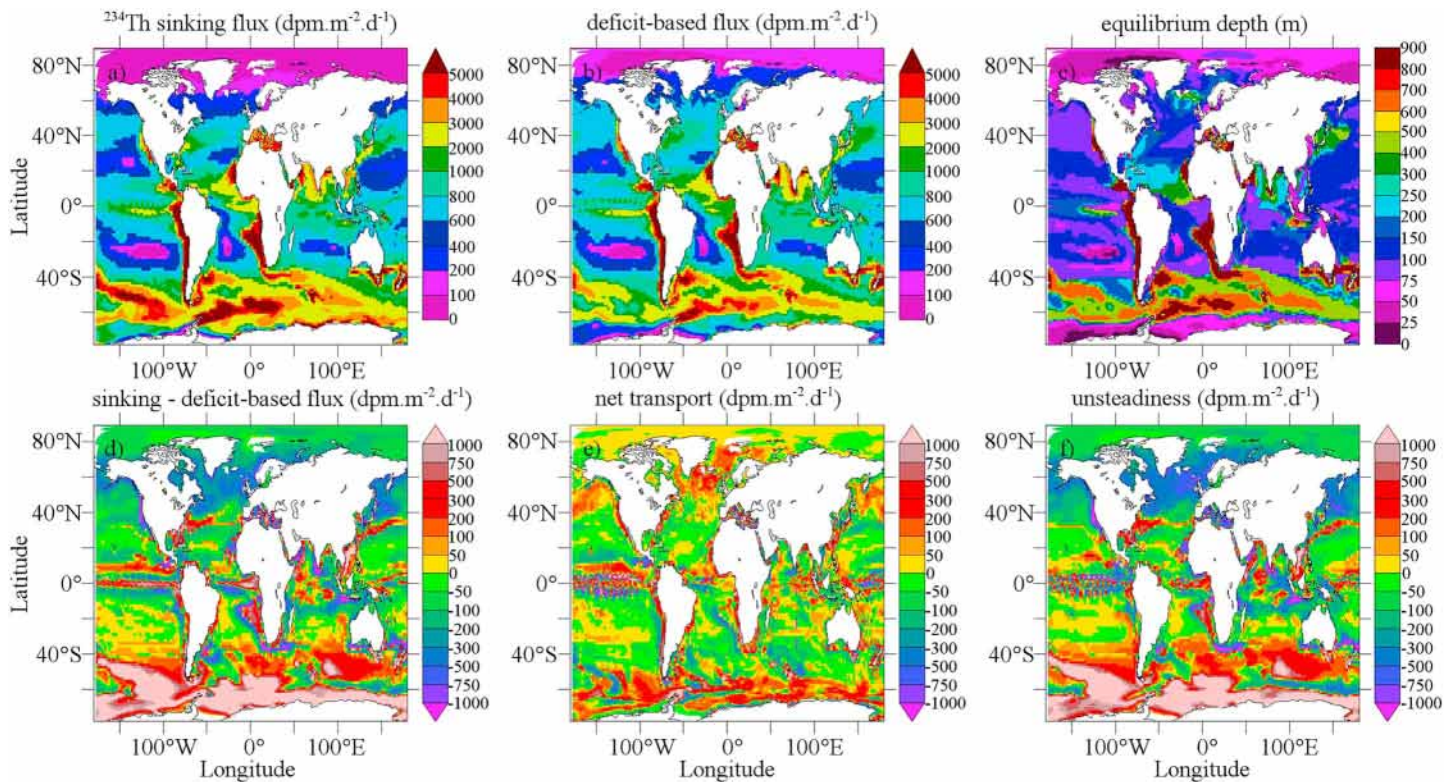
Figure 14. Model ^{234}Th sinking flux (a), 1-D deficit-based estimates (b), and their differences (d) at the equilibrium depth (c) at the solstice of December. The difference is caused by transport (e) and unsteadiness (f). The partition coefficients after inversion TPZM are used in this simulation.

regions, SS model fluxes also differ from sinking fluxes, in a rather unpredictable way. The difference can reach values up to $\pm 1,000$ dpm·m^{-2}·day^{-1}. Therefore, in upwelling regions, vertical advection should be estimated if possible before applying a carbon export steady-state or, preferentially, a nonsteady-state model, especially if the upwelling is seasonal. Still, according to Le Moigne et al. (2013), most carbon export studies assume steady state and neglect transport, even in regions where biases are large.

These findings are consistent with the few previous estimates of time variability and transport at local scales. For instance, Martin et al. (2011) showed at one location in the North Atlantic, in May 2008, during a diatom bloom, that the carbon export flux estimated by a steady-state model was only 20% of the total flux. Buesseler et al. (1995) and Bacon et al. (1996) showed that carbon fluxes in the Equatorial Pacific were underestimated by 30% to 40% just by neglecting the upwelling (vertical advection). Transport is also known to have a major effect on ^{234}Th activities at small scales not represented in our 2° model. Resplandy et al. (2012) showed in a 1/54° numerical model of the North Atlantic that mesoscale and submesoscale ocean dynamics induced a large variability of surface ^{234}Th activity, in the range from 270 to 550 dpm/m^3, at a spatial scale of only 1°.

4.3. Particle Export and ^{234}Th Inverse Modeling

In our study, partition coefficients are constrained by observations of ^{234}Th activity, which is mainly controlled by export. But the ^{234}Th export rate (S) also depends on other parameters, as shown in equations (6) and (7):

$$S = \sum_p \frac{\partial(Th_p w_p)}{\partial z} = \sum_p \frac{\partial(C_p K_p^d Th_d w_p)}{\partial z}. \tag{17}$$

In the above equation, K_p^d and the particle export flux $C_p w_p$ have the same effect, meaning that total ^{234}Th activity cannot be used to constrain one of these parameters independently from the other. Total thorium observations can be used to constrain the export flux $C_p w_p$ when a precise estimate or measurement of K_p^d (replaced by the C:^{234}Th ratio in BCP studies) is available. But the discussion in section 4.1 has shown that K_p^d values of the different particle types are poorly known. As shown by equation (7), particulate ^{234}Th

$(\sum\limits_{p} C_p K_p^d Th_d)$ is affected in the same way by K_p^d and C_p, but w_p only has an indirect effect through its influence on C_p and Th_d. This means particulate [234]Th contains a complementary information on w_p but still cannot be used to constrain K_p^d independently from C_p. In fact, equation (17) shows that a rigorous approach should be based on a nonlinear inversion, which is a computationally heavy task, needing much more data than presently available. Here we tackle the problem in a nonconventional way, by assuming in fact that the K_p^ds are much less well known than the export fluxes obtained from a 3-D simulation. Considering the range of the K_p^d values in the literature, this statement makes sense. Nevertheless, as this model export flux is obviously not perfect, we address now the confidence we can put in the inversion.

An example of bias in partition coefficients estimates caused by errors in the model (e.g., particle concentrations) is given by Dutay et al. (2009). These authors modeled another isotope of thorium, [230]Th, using a previous version of PISCES, without variable lability. As a consequence, sPOC was remineralized too fast and was in very low concentration below the euphotic layer compared to observations. Dutay et al. (2009) found that having the same partition coefficient on sPOC and bPOC was not satisfactory, as it failed to produce enough particulate [230]Th. They managed to better fit observations by imposing an extremely high K_p^d for sPOC, 10^9, as opposed to 10^6 for bPOC. A higher K_p^d is compatible with our findings, but $K_p^d = 10^9$ appears unrealistically high and inconsistent with any other study, as was acknowledged by the authors. In our inversions, K_p^d estimates for sPOC are rather 2 to 4 times higher than for bPOC and cal and remains within the range of published studies. This result highlights the improvement brought to PISCES by the POC lability continuum (Aumont et al., 2017).

In our inversion, errors in the concentrations (C_p) and sinking speeds (w_p) of particles, or in the parameterization of [234]Th behavior, might bias our estimates of partition coefficients. For instance, sPOC, bPOC, cal, and bSi would have very similar K_p^d values if PISCES overestimated bSi and underestimated sPOC export twofold. This would be enough to make our results spurious, showing the importance of using validated particle concentrations. Equation (17) also shows that an increase in particle sinking speed with depth would have a similar effect on total [234]Th to an increase in K^d, reducing deep [234]Th activities. Depth-dependent sinking speed has already been proposed by Berelson (2002) based on observations. If this assumption is accurate, K_p^ds would not need to increase so much with depth.

The comparison of inversions with (TZM and TPZM) and without (TZ and TPZ) concentration correction below 100 m gives another example of errors still existing in the distribution of particles and how they can bias inversion results. Replacing particle concentrations deeper than 100 m by power law profiles closer to observations (with bSi and cal decreasing much faster with depth) increased the partition coefficient of fast-sinking particles at depth dramatically. bSi K_p^d estimates at depth was even multiplied by 7, from $0.27\text{–}1.90 \times 10^6$ to $4.38\text{–}11.4 \times 10^6$. We consider the new values to be more realistic because they are based on more realistic particle concentrations and because they make bSi more similar to the other particles, which all adsorb more thorium at greater depths. However, the profile correction is empirical. Further improvement in PISCES cal and bSi dynamics (especially remineralization) is required to correct this bias in a more mechanistic way.

Biases can also stem from the [234]Th modeling framework itself. The results of an inversion procedure (here the estimates of the partition coefficients) depend on the model design and on the assumptions which have been used to build it. For instance, our model results show that assuming a constant and uniform partition coefficient for each phase does not represent the reality accurately. Indeed, this study has revealed that in order to recover [234]Th activities deeper than 100 m, partition coefficients have to increase with depth. Other modes of K_p^d variability, not represented in our model, exist. For instance, according to Honeyman and Santschi (1989), partition coefficients are higher when particle concentration is lower. In other words, increasing particle concentration does not increase the ratio of particulate to dissolved thorium in a proportional way. Variations in partition coefficients with both depth and particle concentration could be represented in a mechanistic way by implementing an explicit description of thorium adsorption (k_1) and desorption (k_{-1}) in our model (Lerner et al., 2017; Marchal & Lam, 2012). In this alternative model, sinking particles would continuously adsorb [234]Th on their way, accounting for the depth dependence of K_p^d without adding any degree of freedom (K_p^d for surface and deep ocean in our approach and k_1 and k_{-1} for the adsorption/desorption model). Explicit adsorption would also reproduce the dependence of K_p^d on particle concentrations, since the processes creating and consuming particles in PISCES are slow in particle-poor regions such as subtropical gyres. Several thorium isotopes could be used together to constrain k_1 and k_{-1}.

Indeed, thorium isotopes are expected to have the same k_1 and k_{-1}, which are related to their chemistry only, but not the same K^ds, which also depend on their half-lives. Thorium-230, a long studied isotope, contains complementary information at larger time scales and at greater depth because of its very low radioactivity. Based on this improved Th model, inverse modeling able to constrain sinking speed, particle aggregation, disaggregation, and dissolution rates already exist (Clegg & Whitfield, 1991; Lerner et al., 2017; Marchal & Lam, 2012; Murnane et al., 1994). They have been used in simplified configurations (unidimensional on the vertical direction and generally no more than two particle types). With more data, including concentrations of several particle types, a possible future improvement could be to extend this approach to 3-D time-dependent models by constraining some particle dynamics parameters, thus providing a better description of the BCP. Nevertheless, a full inverse 3-D modeling aiming to estimate k_1 and k_{-1} cannot use the approximation of equation (7), and the thorium activities in all phases must be simulated by the model. Therefore, the computation time and storage of such an inversion is dramatically enhanced, all the more since other parameters, such as w, are also estimated.

None of the inversions performed in this study were able to explain more then 45.8% of the total ^{234}Th variance, and the decrease in the residuals observed for each new inversion—from one unique K^d to several K_p^d associated with particle types and from a uniform K_p^d to a K_p^d varying with depth—is rather small. Measurement errors are significant but cannot account for all the residuals. When error estimates for total ^{234}Th measurements are provided, they most often lie between 50 and 200 dpm/m^3. Errors for particulate ^{234}Th are generally lower than 50 dpm/m^3. As a matter of fact, rather than a decrease of the norm of the residuals, the improvements of the successive inversions come from the reduction of systematic biases, such as in the intermediate depths.

As already pointed out, the NEMO/PISCES model can exhibit regional biases. The final inversion has corrected most of the discrepancies in the vertical structure of several particle type profiles. Nevertheless, drawbacks in the horizontal gradients are still existing in the present simulation, such as in the Eastern Pacific Ocean. Unresolved by our relatively low resolution (2°) model, mesoscale and submesoscale eddies are another potential source of error. The 1/54° North Atlantic model of Resplandy et al. (2012) showed a variability of 270 to 550 dpm/m^3 at spatial scales of only 1°. This variability is similar to our rmse of total ^{234}Th after inversion, which is never smaller than 336.7 dpm/m^3. High spatial variability is also common in observations. As an example, Newton et al. (1994) noted in 1990 that a phytoplankton bloom was recorded at one site and not at a second site around 100 km away, so close that the two sites would have been on the same cell of our model. Moreover, Newton et al. (1994) showed with sediment traps that the average carbon export at a given location of the northeast Atlantic was four times higher in 1989 than in 1990 and had a different distribution in time. As it is absent from the particle fields used in this study, interannual variability in ^{234}Th activity cannot be recovered and is yet another important source of error. Unexplained variability of the same order of magnitude exist on carbon export efficiency and its variability, affecting current estimates of the BCP (Buesseler et al., 2007; Henson et al., 2015; Sanders et al., 2014). Finally, the high level of the final residuals of our inversion can also be linked to the "model aggregation" issue (Vallino, 2000). Due to the extreme complexity of biological and chemical systems, models always simplify the reality, aggregating different species or particles into a single compartment. PISCES has only four plankton types and five particle types, which is certainly too elementary to capture the richness of the system. Increasing the model complexity nevertheless requires both more observations and complementary knowledge on the considered processes. Otherwise, the decrease of the residuals might be artificial, resulting only from a large number of badly constrained degrees of freedom.

5. Conclusions

Using an inverse modeling technique based on a 3-D time-dependent circulation and biogeochemistry model (NEMO-PISCES), we were able to estimate the partition coefficients of thorium-234 for five different classes of particles, including plankton, bSi, lithogenic dust, sPOC, and a class composed of both bPOC and cal, two particle types with too similar distributions in PISCES to have their partition coefficients determined separately. Our partition coefficient estimates lie between 0.26×10^6 and 187×10^6. Whatever the cost function used, sPOC and lithogenic particles have the highest partition coefficients, and bSi has the lowest one. We showed that a scavenging model with a single partition coefficient could not properly recover ^{234}Th observations deeper than 100 m. Partition coefficient should at least vary with depth, in which case they are

3 to 14 times higher at 1,000 m than near the surface. Depth dependence might also occur for other scavenged TEIs. Inversion results are strongly dependent on the underlying model of particle dynamics. This was shown by replacing PISCES particle concentration below 100 m by power law decreasing functions that are closer to observations, especially for the unvalidated cal and bSi. Large changes in K_p^d estimates occurred, including an increase by one order of magnitude for bSi, evidencing that progress still has to be made on particle dynamics modeling. Discrepancies between model and data remain quite high: No inversion managed to reduce the root mean square of residuals below 336.7 dpm/m^3 or to explain more than 45.8% of total ^{234}Th variance. This is the order of magnitude of perturbations caused by mesoscale and submesoscale eddies not represented by our 2° model, but measurement errors, typically between 50 and 200 dpm/m^3 for total ^{234}Th and less than 50 dpm/m^3 for particulate ^{234}Th, are also significant.

Our results can be used to quantify systematic biases associated with common assumptions made by ^{234}Th-based estimates of the BCP. Carbon export estimates often assume that only particles larger than 53 μm sink. However, in our model, because of its high partition coefficient and high concentration and despite sinking at only 2 m/day, small particulate organic carbon was found to account for 30% of global ^{234}Th export at equilibrium depth and up to 90% in subtropical gyres. Using the relatively high carbon to thorium ratio of larger particles to compute carbon export then leads to overestimating the BCP by up to 100%. Carbon export models usually also neglect transport (advection and diffusion) and assume steady state. We showed that, with the K_p^d values of our most elaborate inversion, the error made by these two simplifications could be high, although they depend on time and location. At high latitudes at the beginning of the phytoplankton bloom, the sinking flux is regularly underestimated by more than 1,000 dpm·m^{-2}·day^{-1}. In some cases, fluxes are underestimated by up to 50%.

In a near future, GEOTRACES cruises from all the oceans and all times of the year will make our K_p^d estimates representative of a broader range of oceanographic conditions. Models could also be improved in other ways. More in situ measurements of ^{234}Th on several standardized size classes of particles, including colloids, could be used to constrain a more detailed ^{234}Th model, where ^{234}Th fluxes between different phases would be explicitly considered. Several isotopes could be used for this purpose as they share the same chemical properties and thus the same adsorption and desorption rates but contain complementary information on different time scales and depths due to their different half-lives. Moreover, thorium isotopes contain information on particle dynamics, including the BCP. Some model parameters related to particles can be recovered by combining thorium isotopes with measurements of particle concentrations, as already done by 1-D studies. Nevertheless, measurement errors and sampling biases due to small-scale ocean dynamics, as well as simplifications used (and needed) in modeling, raise important issues, which could make difficult a significant decrease in the residuals between model results and observations in a 4-D ocean below 300 dpm/m^3.

Appendix A: Error Statistics

This section describes the method used to estimate thorium-234 (^{234}Th) partition coefficients and their errors.

The inverse problem is the following one. Oceanic ^{234}Th activity is measured at n points of space and time. A numerical model, based on an ocean general circulation model (NEMO-OPA) and a biogeochemistry model (PISCES), outputs ^{234}Th activity at the same points. Model results depend on p unknown parameters, the partition coefficients. There is one partition coefficient for each class or particle or two in the depth-dependent version. The goal of the inverse technique is to find the partition coefficients minimizing the distance between modeled and observed ^{234}Th activities.

Let us call $\vec{k}$ the vector of all partition coefficients and k_j the jth partition coefficient. Let us call o_i and m_i the observed and modeled ^{234}Th activities at the ith observation point and $\vec{o}$ and $\vec{m}$ the corresponding vectors. The distance between model and observations is represented in a scalar, the cost function C. In our study, C is a least-squares cost function: It is the sum of the squared distances between each observation and the corresponding model thorium.

$$C(\vec{k}) = \sum_{i=1}^{n}(m_i(\vec{k}) - o_i)(m_i(\vec{k}) - o_i) = (\vec{m}(\vec{k}) - \vec{o})^{\top}(\vec{m}(\vec{k}) - \vec{o}). \tag{A1}$$

This inverse problem is nonlinear in the unknowns: [234]Th activity is not proportional to partition coefficients. Nevertheless, $\vec{m}$ is a differentiable function of $\vec{k}$, so that it can be linearized around a first estimate $\vec{k}_0$ by using the Jacobian matrix of $\vec{m}$, noted $\mathbf{J}$.

$$\vec{m}(\vec{k}) = \vec{m}(\vec{k}_0) + \mathbf{J}_{\vec{k}_0}(\vec{k} - \vec{k}_0) + \vec{\epsilon}. \tag{A2}$$

$\vec{\epsilon}$ is the nonlinear term. It is negligible term when $(\vec{k} - \vec{k}_0)$ is small enough. The cost function can then be written as in a least-squares problem:

$$C(\vec{k}) = (\mathbf{J}_{\vec{k}_0}\vec{\delta k} - \vec{b})^{\top}(\mathbf{J}_{\vec{k}_0}\vec{\delta k} - \vec{b}), \tag{A3}$$

$$\vec{\delta k} = \vec{k} - \vec{k}_0, \tag{A4}$$

$$\vec{b} = \vec{o} - \vec{m}(\vec{k}_0). \tag{A5}$$

The gradient of the cost function near $\vec{k}_0$ is

$$\vec{\nabla}C(\vec{\delta k}) = 2\mathbf{J}_{\vec{k}_0}^{\top}(\mathbf{J}(\vec{k}_0)\vec{\delta k} - \vec{b}). \tag{A6}$$

The cost function approximate has to be minimal at the optimal δk, called δk_1, which means that the gradient has to be zero:

$$\vec{\nabla}C(\vec{\delta k}_1) = 2\mathbf{J}_{\vec{k}_0}^{\top}(\mathbf{J}(\vec{k}_0)\vec{\delta k}_1 - \vec{b}) = \vec{0}. \tag{A7}$$

As $n > p$, the problem is overdetermined. Then, by assuming that $\mathbf{J}_{\vec{k}_0}^{\top}\mathbf{J}_{\vec{k}_0}$ is invertible (nonsingular):

$$\vec{\delta k}_1 = \mathbf{J}_{\text{inv}}(\vec{k}_0)\vec{b}, \tag{A8}$$

$$\mathbf{J}_{\text{inv}}(\vec{k}_0) = (\mathbf{J}(\vec{k}_0)^{\top}\mathbf{J}(\vec{k}_0))^{-1}\mathbf{J}(\vec{k}_0)^{\top}. \tag{A9}$$

Matrix $\mathbf{J}_{\text{inv}}$ is the pseudo-inverse of $\mathbf{J}$, transforming the consequences into their most probable causes and justifying the word "inversion." Equation (A8) corresponds to (2.95) in Wunsch (2006).

However, the partition coefficients of vector $\vec{k}_1$ are not optimal, because an approximation is made when assuming the Jacobian is constant and the higher order terms are equal to zero. In order to improve the guess, the problem can be linearized again around $\vec{k}_1 = \vec{k}_0 + \vec{\delta k}_1$. A new iteration is then performed and so on. The nth iteration consists in

$$\vec{k}_n = \vec{k}_{n-1} + (\mathbf{J}(\vec{k}_{n-1})^{\top}\mathbf{J}(\vec{k}_{n-1}))^{-1}\mathbf{J}(\vec{k}_{n-1})^{\top}(\vec{o} - \vec{m}(\vec{k}_{n-1})). \tag{A10}$$

Iterations stop when reaching a convergence criterion. Our iterations are stopped when that the relative reduction in the sum of squares is lower than 10^{-5}. In practice, no more than 10 iterations are needed, as the problem is close enough to linearity.

The uncertainties in the estimated partition coefficients $(\vec{k})$ resulting from errors on observations $(\vec{o})$ are derived from the posterior covariance matrix. The posterior covariance matrix is computed at the last iteration, in the same way as in a least-squares problem, using the Jacobian at the solution. A few transformations are useful to understand the problem better. Matrix $\mathbf{H}$ is defined by

$$\mathbf{H} = \mathbf{J}(\mathbf{J}^{\top}\mathbf{J})^{-1}\mathbf{J}^{\top} = \mathbf{J}\mathbf{J}_{\text{inv}}.$$

As $\mathbf{H}^2 = \mathbf{H}^{\top} = \mathbf{H}$, $\mathbf{H}$ is an orthogonal projector on a subspace of dimension p. As $\mathbf{J}\vec{\delta k}_{\text{opt}} = \mathbf{H}\vec{b}$, the model concentration is the projection of the observations on this subspace, whereas the vector of residuals is the projection on the complementary subspace.

Simple algebraic transformations yield

$$\mathbf{HJ} = \mathbf{J}(\mathbf{J^T J})^{-1}\mathbf{J^T J} = \mathbf{J},$$ (A11)

$$\mathbf{J_{inv}J} = (\mathbf{J^T J})^{-1}\mathbf{J^T J} = \mathbf{I_p},$$ (A12)

$$\mathbf{J_{inv}J_{inv}^T} = (\mathbf{J^T J})^{-1}\mathbf{J^T J}(\mathbf{J^T J})^{-1} = (\mathbf{J^T J})^{-1}.$$ (A13)

This least-squares method does not weight observations, and assume observations are not correlated, as expressed by its simple cost function. As a result, the error covariance of $\mathbf{J}\vec{\delta x} - \vec{b}$, called prior error covariance, is considered to be a constant diagonal matrix:

$$\langle(\mathbf{J}\vec{\delta k} - \vec{b})(\mathbf{J}\vec{\delta k} - \vec{b})^\top\rangle = \sigma^2 \mathbf{I_n}.$$ (A14)

In the above equation, the angle brackets represent the expected value. The posterior covariance matrix of $\vec{\delta k}$ is

$$
\begin{aligned}
\mathbf{V_{kk}} &= \langle(\vec{\delta k} - \vec{\delta k_{opt}})(\vec{\delta k} - \vec{\delta k_{opt}})^\top\rangle \\
&= \langle(\mathbf{J_{inv}}\mathbf{J}\vec{\delta k} - \mathbf{J_{inv}}\vec{b})(\mathbf{J_{inv}}\mathbf{J}\vec{\delta k} - \mathbf{J_{inv}}\vec{b})^\top\rangle \\
&= \mathbf{J_{inv}}\langle(\mathbf{J}\vec{\delta k} - \vec{b})(\mathbf{J}\vec{\delta k} - \vec{b})^\top\rangle\mathbf{J_{inv}^T} \\
&= \sigma^2 \mathbf{J_{inv}J_{inv}^T}.
\end{aligned}
$$ (A15)

Equation (A3) corresponds to (2.102) in Wunsch (2006). σ^2 is related to the mean square of residuals v_η the following way:

$$
\begin{aligned}
v_\eta &= \langle(\mathbf{J}\vec{k_{opt}} - \vec{b})^\top(\mathbf{J}\vec{k_{opt}} - \vec{b})\rangle \\
&= \langle(\mathbf{H}\vec{b} - \vec{b})^\top(\mathbf{H}\vec{b} - \vec{b})\rangle \\
&= \langle((\mathbf{I_n} - \mathbf{H})(\mathbf{J}\vec{\delta k} - \vec{b}) + (\mathbf{HJ} - \mathbf{J})\vec{\delta k})^\top((\mathbf{I_n} - \mathbf{H})(\mathbf{J}\vec{\delta k} - \vec{b}) + (\mathbf{HJ} - \mathbf{J})\vec{\delta k})\rangle \\
&= \langle(\mathbf{J}\vec{\delta k} - \vec{b})^\top(\mathbf{I_n} - \mathbf{H})(\mathbf{J}\vec{\delta k} - \vec{b})\rangle \\
&= \sigma^2 \frac{n-p}{n}.
\end{aligned}
$$ (A16)

Then, using equations (A12), (A14), and (A15), we can compute V_{xx}:

$$\mathbf{V_{xx}} = \frac{n}{n-p}v_\eta(\mathbf{J^T J})^{-1}.$$ (A17)

The diagonal terms of V_{xx} are the squared uncertainties on $\vec{k}_{opt}$, whereas the other terms are covariances, indicating partition coefficients with similar effects. Very high or very low covariances indicate parameters having very similar effect on ^{234}Th distribution. These partition coefficients cannot be inverted together.

Two cost functions are used in this study. Their only difference is the use of particulate ^{234}Th or not, which does not change the principle of the inversion. The methods presented in this appendix apply to both cases.

Appendix B: Particle Concentration Correction Scheme Below 100 m Deep

The results of the ^{234}Th scavenging model depend on the particle distribution. PISCES particle concentrations are used in five of the seven inversions presented in this study. As a result, errors in PISCES could bias partition coefficient estimates. The two remaining inversions intend to correct for the effect of some known biases of PISCES by replacing particle concentrations below 100 m by a data-constrained power function. This section describes these biases and explains how the new particle distributions are built.

Model particle concentrations were compared to particle observations from three sources. Lam et al. (2011) have compiled a global data set of sPOC (<53 μm) and bPOC (>53 μm), cal, and bSi. Some GEOTRACES cruises (Data Set S1) also have measurements of bSi and cal, and some studies of our data set (Data Set S1)
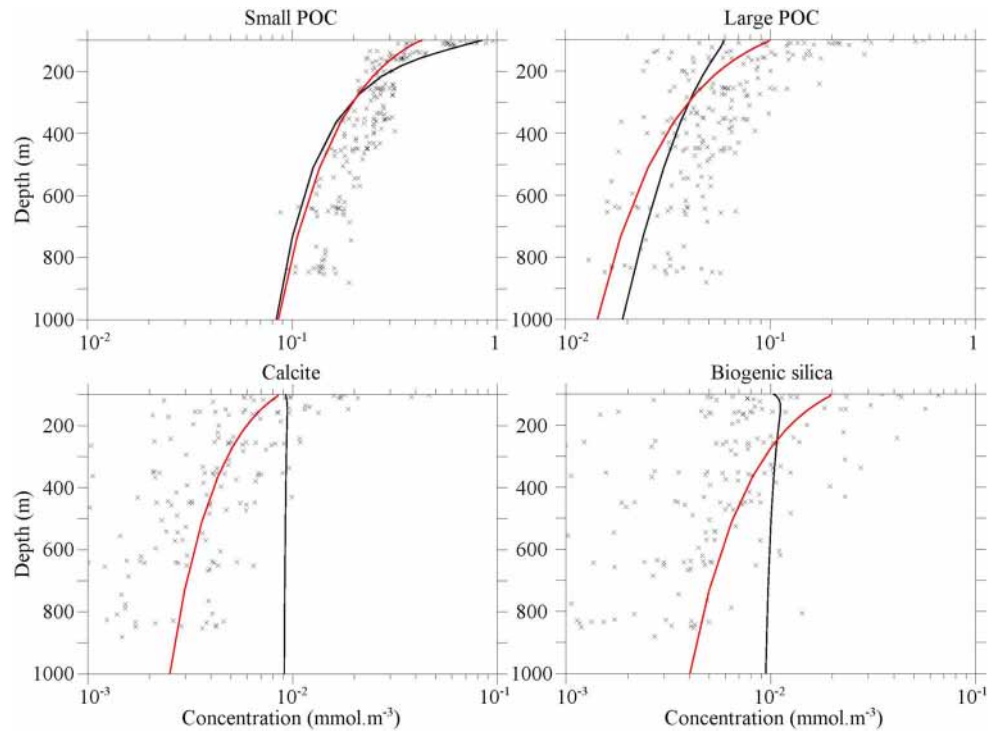
Figure B1. Equatorial Pacific concentrations of small POC, large POC, calcite, and biogenic silica. Black lines represent average Pelagic Interactions Scheme for Carbon and Ecosystem Studies concentrations at each depth, red lines represent corrected concentrations, and crosses are observations. POC = particulate organic carbon.

have measured the two size classes of organic carbon. It turns out that the shape of PISCES particle profiles does not perfectly correspond to the observations between 100 and 1,000 m deep. In spite of the variable lability parameterization (Aumont et al., 2017), sPOC still decreases too fast with depth. But the largest discrepancies occur for cal and bSi: The dissolution of these particles is very slow in the model, producing near constant profiles with depth, whereas, in the observations, their concentrations decrease in a similar way to particulate organic carbon. The two last inversions, TZM and TPZM, are designed to estimate the biases on TP and TPZ partition coefficients induced by these misfits. sPOC, bPOC, cal, and bSi concentrations between 100 and 1,000 m deep are corrected. Model particle concentrations are kept the same as PISCES in the upper 100 m and are replaced below this depth by power law functions of depth, which is the most widespread way to describe particle vertical fluxes below the euphotic layer since (Martin et al., 1987). In our model, sinking speeds are constants, so that correcting concentrations is equivalent to correcting vertical fluxes. The corrected concentration for particle type p is then

$$P_{\text{cor}} = a_p P_{\text{pisces}}^{z=100} \quad (z/100)^{b_p} \quad v(100\,\text{m} < z < 1,000\,\text{m}). \tag{B1}$$

Two global constants, a_p and b_p, have to be determined. This is done by two successive least-squares minimization steps. The first constant, a_p, is a normalizing factor to make the model concentrations at 100 m similar to the observations. It is determined by a least-squares method: The differences (on a logarithmic scale) between $a_p P_{\text{pisces}}$ and observations between 70 and 140 m deep are minimized. The second constant, b_p, is the exponent of the power law, representing the shape of the profile. In the second step, a_p is set to the value determined during the first step, and b_p is determined by minimizing the following cost function for each particle class:

$$C_{\text{pow}}^p(b_p) = \sum_{100<z<1,000} \left(\log(a_p P_{\text{pisces}}^{z=100}(z/100)^{b_p}) - \log(P_{\text{obs}}) \right)^2. \tag{B2}$$

The second step cannot be made before a_p is determined because spurious correction for biases around 100 m would occur. As an illustration, model particle concentrations in the equatorial Pacific before and

after correction are shown in Figure B1 and compared with observations. Profile correction significantly improve cal and bSi concentrations at depth. Eventually, for comparability with the previous simulations and because size classes of PISCES and observations do not exactly match, the normalizing factors (a_p) were removed from the final corrected concentrations, and only the exponents (b_p), which are linked to remineralization/dissolution rates, were used. The corrected concentrations below 100 m deep are the following:

$$sPOC_{\text{cor}} = sPOC_{\text{pisces}}^{z=100} \ (z/100)^{-0.697}, \tag{B3}$$

$$bPOC_{\text{cor}} = bPOC_{\text{pisces}}^{z=100} \ (z/100)^{-0.854}, \tag{B4}$$

$$cal_{\text{cor}} = cal_{\text{pisces}}^{z=100} \ (z/100)^{-0.539}, \tag{B5}$$

$$bSi_{\text{cor}} = bSi_{\text{pisces}}^{z=100} \ (z/100)^{-0.704}. \tag{B6}$$

After this profile correction, the concentrations of all particle types decrease significantly with depth. This might change partition coefficients after inversion and avoid spurious results.

References

Amiel, D., Cochran, J. K., & Hirschberg, D. J. (2002). ^{234}Th/^{238}U disequilibrium as an indicator of the seasonal export flux of particulate organic carbon in the North Water. *Deep Sea Research Part II:*, *49*, 5191–5209. https://doi.org/10.1016/S0967-0645(02)00185-6

Aumont, O., Éthé, C., Tagliabue, A., Bopp, L., & Gehlen, M. (2015). PISCES-v2: An ocean biogeochemical model for carbon and ecosystem studies. *Geoscientific Model Development*, *8*, 2465–2513. https://doi.org/10.5194/gmd-8-2465-2015

Aumont, O., van Hulten, M., Roy-Barman, M., Dutay, J.-C., Éthé, C., & Gehlen, M. (2017). Variable reactivity of particulate organic matter in a global ocean and biogeochemical model. *Biogeosciences*, *14*, 2321–2341. https://doi.org/10.5194/bg-14-2321-2017

Bacon, M. P., Cochran, J. K., Hirschberg, D., Hammar, T. R., & Fleer, A. P. (1996). Export flux of carbon at the equator during the EqPac time-series cruises estimated from ^{234}Th measurements. *Deep Sea Research Part II: Topical Studies in Oceanography*, *43*, 1133–1153. https://doi.org/10.1016/0967-0645(96)00016-1

Bacon, M., & Rutgers van der Loeff, M. M. (1989). Removal of thorium-234 by scavenging in the bottom nepheloid layer of the ocean. *Earth and Planetary Science Letters*, *92*, 157–164. https://doi.org/10.1016/0012-821X(89)90043-5

Berelson, W. M. (2002). Particle settling rates increase with depth in the ocean. *Deep Sea Research Part II: Topical Studies in Oceanography*, *49*, 237–251. https://doi.org/10.1016/S0967-0645(01)00102-3

Bishop, J. K. B., Edmond, J. M., Ketten, D. R., Bacon, M. P., & Silker, W. B. (1977). The chemistry, biology, and vertical flux of particulate matter from the upper 400m of the equatorial Atlantic Ocean. *Deep-Sea Research and Oceanographic Abstracts*, *24*, 511–548.

Buesseler, K. O. (2003a). Thorium 234 in particulate and dissolved phases; POC/PON. https://doi.org/10.1594/PANGAEA.116321

Buesseler, K. O. (2003b). Thorium 234 in particulate and dissolved phases, POC and PON from pump cast NBP96-04A-01-4. https://doi.org/10.1594/PANGAEA.129181

Buesseler, K. O. (2003c). Thorium 234 activity in particulate and dissolved phases at station AT_II-119/4_4-1. https://doi.org/10.1594/PANGAEA.112051

Buesseler, K., Andrews, J. A., Hartman, M. C., Belastock, R., & Chai, F. (1995). Regional estimates of the export flux of particulate organic carbon derived from thorium-234 during the JGOFS EqPac program. *Deep Sea Research Part II: Topical Studies in Oceanography*, *42*, 777–804. https://doi.org/10.1016/0967-0645(95)00043-P

Buesseler, K., Ball, L., Andrews, J., Benitez-Nelson, C., Belastock, R., Chai, F., & Chao, Y. (1998). Upper ocean export of particulate organic carbon in the Arabian Sea derived from thorium-234. *Deep Sea Research Part II: Topical Studies in Oceanography*, *45*, 2461–2487. https://doi.org/10.1016/S0967-0645(98)80022-2

Buesseler, K. O., Benitez-Nelson, C. R., Moran, S. B., Burd, A., Charette, M., Cochran, J. K., et al. (2006). An assessment of particulate organic carbon to thorium-234 ratios in the ocean an their impact on the application of ^{234}Th as a POC flux proxy. *Marine Chemistry*, *100*, 213–233. https://doi.org/10.1016/j.marchem.2005.10.013

Buesseler, K. O., Lamborg, C. H., Boyd, P. W., Lam, P. J., Trull, T. W., Bidigare, R. R., et al. (2007). Revisiting carbon flux through the ocean's twilight zone. *Science*, *316*, 567–570. https://doi.org/10.1126/science.1137959

Buesseler, K. O., Pike, S., Maiti, K., Lamborg, C. H., Siegel, D. A., & Trull, T. W. (2009). Thorium-234 as a tracer of spatial, temporal and vertical variability in particle flux in the North Pacific. *Deep Sea Research Part I: Oceanographic Research Papers*, *56*, 1143–1167. https://doi.org/10.1016/j.dsr.2009.04.001

Burd, A. B., Jackson, G. A., & Moran, S. B. (2007). The role of the particle size spectrum in estimating POC fluxes from ^{234}Th/^{238}U disequilibrium. *Deep Sea Research Part I: Oceanographic Research Papers*, *54*, 897–918. https://doi.org/10.1016/j.dsr.2007.03.006

Burd, A. B., Moran, S. B., & Jackson, G. A. (2000). A coupled adsorption-aggregation model of the POC/^{234}Th ratio of marine particles. *Deep Sea Research Part I: Oceanographic Research Papers*, *47*, 103–120. https://doi.org/10.1016/S0967-0637(99)00047-3

Cai, P., Rutgers van der Loeff, M., Stimac, I., Nöthig, E.-M., Lepore, K., & Moran, S. B. (2010). Low export flux of particulate organic carbon in the central Arctic Ocean as revealed by ^{234}Th:^{238}U disequilibrium. *Journal of Geophysical Research*, *115*, C10037. https://doi.org/10.1029/2009JC005595

Charette, M. A., & Moran, B. S. (1999). Rates of particle scavenging and particulate organic carbon export estimated using ^{234}Th as a tracer in the subtropical and equatorial Atlantic Ocean. *Deep Sea Research Part II: Topical Studies in Oceanography*, *46*, 885–906. https://doi.org/10.1016/S0967-0645(99)00006-5

Charette, M. A., Moran, S. B., & Bishop, J. K. B. (1999). [234]Th as a tracer of particulate organic carbon export in the subarctic Northeast Pacific Ocean. *Deep Sea Research Part II: Topical Studies in Oceanography*, *46*, 2833–2861. https://doi.org/10.1016/S0967-0645(99)00085-5

Chase, Z., Anderson, R. F., Fleisher, M. Q., & Kubik, P. W. (2002). The influence of particle composition and particle flux on scavenging of Th, Pa and Be in the ocean. *Earth and Planetary Science Letters*, *204*, 215–229. https://doi.org/10.1016/S0012-821X(02)00984-6

Chen, J. H., Edwards, R. L., & Wasserburg, H. J. (1986). [238]U, [234]Th and [232]Th in seawater. *Earth and Planetary Science Letters*, *80*, 241–251. https://doi.org/10.1016/0012-821X(86)90108-1

Chuang, C.-Y., Santschi, P. H., Ho, Y.-F., Conte, M. H., Guo, L., Schumann, D., et al. (2013). Role of biopolymers as major carrier phases of Th, Pa, Pb, Po and Be radionuclides in settling particles from the Atlantic Ocean. *Marine Chemistry*, *157*, 131–143. https://doi.org/10.1016/j.marchem.2013.10.002

Clegg, S. L., & Whitfield, M. (1991). A generalized model for the scavenging of trace metals in the open ocean—II. Thorium scavenging. *Deep Sea Research Part I: Oceanographic Research Papers*, *38*, 91–120. https://doi.org/10.1016/0198-0149(91)90056-L

Coale, K. H., & Bruland, K. W. (1985). [234]Th:[238]U disequilibria within the California Current. *Limnology and Oceanography*, *30*, 22–33. https://doi.org/10.4319/lo.1985.30.1.0022

Cochran, J. K., Buesseler, K. O., Bacon, M. P., Wang, H. W., Hirschberg, D. J., Ball, L., et al. (2000). Short-lived thorium isotopes ([234]Th, [228]Th) as indicators of POC export and particle cycling in the Ross Sea, Southern Ocean. *Deep Sea Research Part II: Topical Studies in Oceanography*, *47*, 3451–3490. https://doi.org/10.1016/S0967-0645(00)00075-8

Cochran, J. R., & Cochran, J. K. (2003). Thorium 234 activity in particulate and dissolved phases at station TT008_5-Pump2. https://doi.org/10.1594/PANGAEA.121475

Coppola, L., & Jeandel, C. (2004). Thorium radionuclides analysed at bottle station ANTARES-IV_004. https://doi.org/10.1594/PANGAEA.140655

Coppola, L., Roy-Barman, M., Wassmann, P., Mulsow, S., & Jeandel, C. (2002). Calibration of sediment traps and particulate organic carbon export using [234]Th in the Barents Sea. *Marine Chemistry*, *80*, 11–26. https://doi.org/10.1016/S0304-4203(02)00071-3

DeVries, T., & Primeau, F. (2011). Dynamically and observationally constrained estimates of water-mass distributions and ages in the global ocean. *Journal of Physical Oceanography*, *41*(12), 2381–2401. https://doi.org/10.1175/jpo-d-10-05011.1

DeVries, T., Primeau, F., & Deutsch, C. (2012). The sequestration efficiency of the biological pump. *Geophysical Research Letters*, *39*, L13601. https://doi.org/10.1029/2012GL

Decho, A. (1990). Microbial exopolymer secretions in ocean environments: Their role(s) in food webs and marine processes. *Oceanography and marine biology*, *28*, 73–153.

Dutay, J.-C., Lacan, F., Roy-Barman, M., & Bopp, L. (2009). Influence of particle size and type on [231]Pa and [230]Th simulation with a global coupled biogeochemical-ocean general circulation model: A first approach. *Geochemistry Geophysics Geosystems*, *10*, Q01011. https://doi.org/10.1029/2008GC002291

Fowler, S. W., & Knauer, G. A. (1986). Role of large particles in the transport of elements and organic compounds through the oceanic water column. *Progress in Oceanography*, *16*, 147–194. https://doi.org/10.1016/0079-6611(86)90032-7

Gehlen, M., Gangstø, R., Schneider, B., Bopp, L., Aumont, O., & Ethe, C. (2007). The fate of pelagic $CaCO_3$ production in a high CO_2 ocean: A model study. *Biogeosciences*, *4*, 505–519. https://doi.org/10.5194/bg-4-505-2007

German, C. R., Fleer, A. P., Bacon, M. P., & Edmond, J. M. (1991). Hydrothermal scavenging at the Mid-Atlantic Ridge: Radionuclide distributions. *Earth and Planetary Science Letters*, *105*, 170–181. https://doi.org/10.1016/0012-821X(91)90128-5

Gloor, M., Gruber, N., Hughes, T. M. C., & Sarmiento, J. L. (2001). Estimating net air-sea fluxes from ocean bulk data. *Global Biogeochemical Cycles*, *15*, 767–782. https://doi.org/10.1029/2000GB001301

Hauglustaine, D. A., Hourdin, F., Jourdain, L., Filiberti, M.-A., Walters, S., Lamarque, J.-F., & Holland, E. A. (2004). Interactive chemistry in the Laboratoire de Météorologie Dynamique general circulation model: Description and background tropospheric chemistry evaluation. *Journal of Geophysical Research*, *109*, D04314. https://doi.org/10.1029/2003JD003957

Hayes, C. T., Anderson, R. F., Fleisher, M. Q., Vivancos, S. M., Lam, P. J., Ohnemus, D. C., et al. (2015). Intensity of Th and Pa scavenging partitioned by particle chemistry in the North Atlantic Ocean. *Marine Chemistry*, *170*, 49–60. https://doi.org/10.1016/j.marchem.2015.01.006

Henson, S. A., Sanders, R., Madsen, E., Morris, P. J., Le Moigne, F., & Quartly, G. D. (2011). A reduced estimate of the strength of the oceans biological carbon pump. *Geophysical Research Letters*, *38*, L04606. https://doi.org/10.1029/2011gl046735

Henson, S. A., Yool, A., & Sanders, R. (2015). Variability in efficiency of particulate organic carbon export: A model study. *Global Biogeochemical Cycles*, *29*, 33–45. https://doi.org/10.1002/2014GB004965

Honeyman, B. D., & Santschi, P. H. (1989). A Brownian-pumping model for oceanic trace metal scavenging: Evidence from Th and isotopes. *Journal of Marine Research*, *47*, 951–992. https://doi.org/10.1357/002224089785076091

JGOFS-INDIA (2002). Radionuclide thorium 234 and salinity measured on water bottle samples during Sagar Kanya cruise SK104. https://doi.org/10.1594/PANGAEA.78699

JGOFS-INDIA (2013). Thorium 234 measured on water bottle samples during Sagar Kanya cruise SK121. https://doi.org/10.1594/PANGAEA.807500

Jacquet, S. H. M., Lam, P. J., Trull, T., & Dehairs, F. (2011). Carbon export production in the subantarctic zone and polar front zone south of Tasmania. *Deep Sea Research Part II: Topical Studies in Oceanography*, *58*, 2277–2292. https://doi.org/10.1016/j.dsr2.2011.05.035

Jeandel, C., Arsouze, T., Lacan, F., Téchiné, P., & Dutay, J.-C. (2007). Isotopic Nd compositions and concentrations of the lithogenic inputs into the ocean: A compilation, with an emphasis on the margins. *Chemical Geology*, *239*(1-2), 156–164. https://doi.org/10.1016/j.chemgeo.2006.11.013

Kawakami, H., & Honda, M. C. (2007). Time-series observation of POC fluxes estimated from [234]Th in the northwestern North Pacific. *Deep Sea Research Part I: Oceanographic Research Papers*, *54*, 1070–1090. https://doi.org/10.1016/j.dsr.2007.04.005

Knauss, K. G., Ku, T.-L., & Moore, W. S. (1978). Radium and thorium isotopes in the surface waters of the east Pacific and coastal Southern California. *Earth and Planetary Science Letters*, *39*, 235–249. https://doi.org/10.1016/0012-821x(78)90199-1

Kwon, E. Y., Kim, G., Primeau, F., Moore, W. S., Cho, H.-M., DeVries, T., et al. (2014). Global estimate of submarine groundwater discharge based on an observationally constrained radium isotope model. *Geophysical Research Letters*, *41*, 8438–8444. https://doi.org/10.1002/2014gl061574

Lam, P., Doney, S. C., & Bishop, J. K. B. (2011). The dynamic ocean biological pump: Insights and from a global and compilation of particulate organic carbon and $CaCO_3$ and opal concentration profiles from the mesopelagic. *Global Biogeochemical Cycles*, *25*, GB3009. https://doi.org/10.1029/2010GB003868

Laws, E. A., Falkowski, P. G., Smith, W. O., Ducklow, H., & McCarthy, J. J. (2000). Temperature effect on export production in the open ocean. *Global Biogeochemical Cycles*, *14*, 1231–1246. https://doi.org/10.1029/1999GB001229

Le Gland, G., Mémery, L., Aumont, O., & Resplandy, L. (2017). Improving the inverse modeling of a trace isotope: How precisely can radium-228 fluxes toward the ocean and submarine groundwater discharge be estimated? *Biogeosciences*, *14*, 3171–3189. https://doi.org/10.5194/bg-14-3171-2017

Le Moigne, F. A. C., Henson, S. A., Sanders, R. J., & Madsen, E. (2013). Global database of surface ocean particulate organic carbon export fluxes diagnosed from the [234]Th technique. *Earth System Science Data*, *5*(2), 295–304. https://doi.org/10.5194/essd-5-295-2013

Lerner, P., Marchal, O., Lam, P. J., Anderson, R. F., Buesseler, K., Charette, M. A., et al. (2016). Testing models of thorium and particle cycling in the ocean using data from station GT11-22 of the U.S. GEOTRACES North Atlantic section. *Deep Sea Research Part I: Oceanographic Research Papers*, *113*, 57–79. https://doi.org/10.1016/j.dsr.2016.03.008

Lerner, P., Marchal, O., Lam, P. J., Buesseler, K., & Charette, M. (2017). Kinetics of thorium and particle cycling along the U.S. GEOTRACES North Atlantic transect. *Deep Sea Research Part I: Oceanographic Research Papers*, *125*, 106–128. https://doi.org/10.1016/j.dsr.2017.05.003

Lin, P., Chen, M., & Guo, L. (2015). Effect of natural organic matter on the adsorption and fractionation of thorium and protactinium on nanoparticles in seawater. *Marine Chemistry*, *173*, 291–301. https://doi.org/10.1016/j.marchem.2014.08.006

Madec, G. (2015). NEMO ocean engine. Note du Pôle de modélisation, Institut Pierre-Simon Laplace (IPSL), France, No 27, ISSN No 1288-1619.

Mahowald, N., Albani, S., Folk, J. F., Engelstaeder, S., Scanza, R., Ward, D. S., & Flanner, M. G. (2014). The size distribution of desert dust aerosols and its impact on the Earth system. *Aeolian Research*, *15*, 53–71. https://doi.org/10.1016/j.aeolia.2013.09.002

Marchal, O., & Lam, P. J. (2012). What can paired measurements of Th isotope activity and particle concentration tell us about particle cycling in the ocean? *Geochimica et Cosmochimica Acta*, *90*, 126–148. https://doi.org/10.1016/j.gca.2012.05.009

Martin, J. H., Knauer, G. A., Karl, D. M., & Broenkow, W. W. (1987). Vertex: Carbon cycling in the Northeast Pacific. *Deep Sea Research Part I: Oceanographic Research Papers*, *34*, 267–285. https://doi.org/10.1016/0198-0149(87)90086-0

Martin, P., Lampitt, R. S., Perry, M. J., Sanders, R., Lee, C., & D'Asaro, E. (2011). Export and mesopelagic particle flux during a North Atlantic spring diatom bloom. *Deep Sea Research Part I: Oceanographic Research Papers*, *58*, 338–349. https://doi.org/10.1016/j.dsr.2011.01.006

Matsumoto, E. (1975). [234]Th-[238]U radioactive disequilibrium in the surface layer of the ocean. *Geochimica et Cosmochimica Acta*, *39*, 205–212. https://doi.org/10.1016/0016-7037(75)90172-6

Mawji, E. e. a (2015). The GEOTRACES intermediate data product 2014. *Marine Chemistry*, *177*, 1–8. https://doi.org/10.1016/j.marchem.2015.04.005

McCave, I. N. (1975). Vertical flux of particles in the ocean. *Deep Sea Research and Oceanographic Abstracts*, *22*, 491–502. https://doi.org/10.1016/0011-7471(75)90022-4

Moore, W. S., Sarmiento, J. L., & Key, R. M. (2008). Submarine groundwater discharge revealed by [228]Ra distribution in the upper Atlantic Ocean. *Nature Geoscience*, *1*(5), 309–311. https://doi.org/10.1038/ngeo183

Moran, S. B., Lomas, M. W., Kelly, R. P., Gradinger, R., Iken, K., & Mathis, J. T. (2012). Seasonal succession of net primary productivity, particulate organic carbon export, and autotrophic community composition in the eastern Bering Sea. *Deep Sea Research Part II: Topical Studies in Oceanography*, *65*, 84–97. https://doi.org/10.1016/j.dsr2.2012.02.011

Moran, S. B., Weinstein, S. E., Edmonds, H. N., Smith, J. N., Kelly, R. P., Pilson, M. E. Q., & Harrison, W. G. (2003). Does [234]Th/[238]U and disequilibrium provide an accurate record of the export flux of and particulate organic carbon from the upper ocean. *Limnology and Oceanography*, *48*, 1018–1029. https://doi.org/10.4319/lo.2003.48.3.1018

Morris, P. J., Sanders, R., Turnewitsch, R., & Thomalla, S. (2007). [234]Th-derived particulate organic carbon export from an island-induced phytoplankton bloom in the Southern Ocean. *Deep-Sea Research II*, *54*, 2208–2232. https://doi.org/10.1016/j.dsr2.2007.06.002

Murnane, R. J., Cochran, J. K., & Sarmiento, J. L. (1994). Estimates of particle- and thorium-cycling rates in the northwest Atlantic Ocean. *Journal of Geophysical Research*, *99*, 3373–3392. https://doi.org/10.1029/93JC02378

Murray, J. W., Downs, J. N., Strom, S., Wei, C.-L., & Jannasch, H. W. (1989). Nutrient assimilation, export production and [234]Th scavenging in the eastern Equatorial Pacific. *Deep Sea Research Part I: Oceanographic Research Papers*, *36*, 1471–1489. https://doi.org/10.1016/0198-0149(89)90052-6

Newton, P. P., Lampitt, R. S., Jickells, T. D., King, P., & Boutle, C. (1994). Temporal and spatial variability of biogenic particle fluxes during the JGOFS northeast Atlantic process studies at 47° N, 20° W. *Deep Sea Research Part I: Oceanographic Research Papers*, *41*, 1617–1642. https://doi.org/10.1016/0967-0637(94)90065-5

Owens, S. A., Pike, S., & Buesseler, K. O. (2014). Thorium-234 as a tracer of particle dynamics and upper ocean export in the Atlantic Ocean. *Deep Sea Research Part II: Topical Studies in Oceanography*, *116*, 42–59. https://doi.org/10.1016/j.dsr2.2014.11.010

Passow, U. (2002). Transparent exopolymer particles (TEP) in aquatic environments. *Progress in Oceanography*, *55*, 287–333. https://doi.org/10.1016/S0079-6611(02)00138-6

Planchon, F., Cavagna, A.-J., André, L., & Dehairs, F. (2013). Late summer particulate organic carbon export and twilight zone remineralisation in the Atlantic sector of the Southern Ocean. *Biogeosciences*, *10*, 803–820. https://doi.org/10.5194/bg-10-803-2013

Puigcorbé, V., Benitez-Nelson, C. R., Masqué, P., Verdeny, E., White, A. E., Popp, B. N., et al. (2015). Small phytoplankton drive high summertime carbon and nutrient export in the Gulf of California and Eastern Tropical North Pacific. *Global Biogeochemical Cycles*, *29*, 1309–1332. https://doi.org/10.1002/2015GB005134

Resplandy, L., Martin, A. P., Le Moigne, F., Martin, P., Aquilina, A., Mémery, L., et al. (2012). How does dynamical spatial variability impact [234]Th-derived estimates of organic export. *Deep Sea Research Part I: Oceanographic Research Papers*, *68*, 24–45. https://doi.org/10.1016/j.dsr.2012.05.015

Richardson, T. L., & Jackson, G. A. (2007). Small phytoplankton and carbon export from the surface ocean. *Science*, *315*, 838–840. https://doi.org/10.1126/science.1133471

Ridgwell, A. J., Watson, A. J., & Archer, D. E. (2002). Modeling the response of the oceanic Si inventory to perturbation, and consequences for atmospheric CO_2. *Global Biogeochemical Cycles*, *16*(4), 1071. https://doi.org/10.1029/2002GB001877

Roca-Martí, M., Puigcorbé, V., Iversen, M. H., Rutgers van der Loeff, M., Klaas, C., Cheah, W., et al. (2017). High particulate organic carbon export during the decline of a vast diatom bloom in the Atlantic sector of the Southern Ocean. *Deep Sea Research Part II: Topical Studies in Oceanography*, *138*, 102–115. https://doi.org/10.1016/j.dsr2.2015.12.007

Roca-Martí, M., Puigcorbé, V., Rutgers van der Loeff, M. M., Katlein, C., Fernández-Méndez, M., & Peeken, I. (2016). Carbon export fluxes and export efficiency in the central Arctic during the record sea-ice minimum in 2012: A joint [234]Th/[238]U and [210]Po/^{210}Pb study. *Journal of Geophysical Research: Oceans*, *121*, 5030–5049. https://doi.org/10.1002/2016JC011816

Rodriguez y Baena, A. M., Boudjenoun, R., Fowler, S. W., Miquel, J. C., Masqué, P., Sanchez-Cabeza, J.-A., & Warnau, M. (2008). [234]Th-based carbon export during an ice-edge bloom: Sea-ice algae as a likely bias in data interpretation. *Earth and Planetary Science Letters*, *269*, 595–603. https://doi.org/10.1016/j.epsl.2008.03.020

Roy-Barman, M., Jeandel, C., Souhaut, M., Rutgers van der Loeff, M., Voege, I., Leblond, N., & Freydier, R. (2005). The influence of particle composition on thorium scavenging in the NE Atlantic Ocean (POMME experiment). *Earth and Planetary Science Letters*, *240*, 681–693. https://doi.org/10.1016/j.epsl.2005.09.059

Rutgers van der Loeff, M. M. (2007). Manual determination of thorium 234 and uranium 238 during cruise ANT-XXIII/3. https://doi.org/10.1594/PANGAEA.615830

Rutgers van der Loeff, M., Cai, P. H., Stimac, I., Bracher, A., Middag, R., Klunder, M. B., & van Heuven, S. M. A. C. (2011). ^{234}Th in surface waters: Distribution of particle export flux across the Antarctic Circumpolar Current and in the Weddell Sea during the GEOTRACES expedition ZERO and DRAKE. *Deep-Sea Research II*, *58*, 2749–2766. https://doi.org/10.1016/j.dsr2.2011.02.004

Sanders, R., Henson, S. A., Koski, M., De La Rocha, C., Painter, S. C., Poulton, A. J., et al. (2014). The biological carbon pump in the North Atlantic. *Progress in Oceanography*, *129*, 200–218. https://doi.org/10.1016/j.pocean.2014.05.005

Santschi, P. H., Guo, L., Walsh, I. D., Quigley, M. S., & Baskaran, M. (1999). Boundary exchange and scavenging of radionuclides in continental margin waters of the Middle Atlantic Bight: Implications for organic carbon fluxes. *Continental Shelf Research*, *19*, 609–636. https://doi.org/10.1016/S0278-4343(98)00103-4

Santschi, P. H., Murray, J. W., Baskaran, M., Benitez-Nelson, C. R., Guo, L. D., Hung, C.-C., et al. (2006). Thorium speciation in seawater. *Marine Chemistry*, *100*, 250–268. https://doi.org/10.1016/j.marchem.2005.10.024

Savoye, N., Benitez-Nelson, C., Burd, A. B., Cochran, J. K., Charette, M., Buesseler, K. O., et al. (2006). ^{234}Th sorption and export models in the water column: A review. *Marine Chemistry*, *100*, 234–249. https://doi.org/10.1016/j.marchem.2005.10.014

Shimmield, G. B., Ritchie, G. D., & Fileman, T. W. (1995). The impact of marginal ice zone processes on the distribution of ^{210}Pb, ^{210}Po and ^{234}Th and implications for new production in the Bellingshausen Sea, Antarctica. *Deep Sea Research Part II: Topical Studies in Oceanography*, *42*, 1313–1335. https://doi.org/10.1016/0967-0645(95)00071-W

Stukel, M. R., & Landry, M. R. (2010). Contribution of picophytoplankton to carbon export in the equatorial Pacific: A reassessment of food web flux inferences from inverse models. *Limnology and Oceanography*, *55*, 2669–2685. https://doi.org/10.4319/lo.2010.55.6.2669

Thomalla, S., Turnewitsch, R., Lucas, M., & Poulton, A. (2006). Particulate organic carbon export from the North and South Atlantic gyres: The ^{234}Th/^{238}U disequilibrium approach. *Deep-Sea Research II*, *53*, 1629–1648. https://doi.org/10.1016/j.dsr2.2006.05.018

Vallino, J. J. (2000). Improving marine ecosystem models: Use of data assimilation and mesocosm experiments. *Journal of Marine Research*, *58*, 117–164. https://doi.org/10.1357/002224000321511223

Vancoppenolle, M., Fichefet, T., Goosse, H., Bouillon, S., Madec, G., & Maqueda, M. A. M. (2009). Simulating the mass balance and salinity of Arctic and Antarctic sea ice. 1. Model description and validation. *Ocean Modelling*, *27*(1-2), 33–53. https://doi.org/10.1016/j.ocemod.2008.10.005

Volk, T., & Hoffert, M. I. (1985). *Ocean carbon pumps: Analysis of relative strengths and efficiencies in ocean-driven atmospheric CO$_2$ changes*, pp. 99–110. Washington, D. C.: American Geophysical Union. https://doi.org/10.1029/GM032p0099

Wohlers, J., Engel, A., Zöllner, E., Breithaupt, P., Jürgens, K., Hoppe, H.-G., et al. (2009). Change in biogenic carbon flow in response to sea surface warming. *Proceedings of the National Academy of Sciences of the United States of America*, *106*, 7067–7072. https://doi.org/10.1073/pnas.0812743106

Wunsch, C. (2006). *Discrete inverse and state estimation problems*. Cambridge: Cambridge University Press.

Young, J., & Murray, J. W. (2003). Isotope activity measured on Go-Flo bottle samples at station TT007_15-GoFlo. https://doi.org/10.1594/PANGAEA.121394

Zhou, K., Nodder, S. D., Dai, M., & Hall, J. A. (2012). Insignificant enhancement of export flux in the highly productive subtropical front, east of New Zealand: A high resolution study of particle export fluxes based on ^{234}Th:^{238}U disequilibria. *Biogeosciences*, *9*, 973–992. https://doi.org/10.5194/bg-9-973-2012